



HAL
open science

Systematic development of upwind numerical fluxes for the space discontinuous Galerkin method applied to elastic wave propagation in anisotropic and heterogeneous media with physical interfaces

B. Tie, A.-S. Mouronval

► To cite this version:

B. Tie, A.-S. Mouronval. Systematic development of upwind numerical fluxes for the space discontinuous Galerkin method applied to elastic wave propagation in anisotropic and heterogeneous media with physical interfaces. *Computer Methods in Applied Mechanics and Engineering*, 2020, 372, pp.113352. 10.1016/j.cma.2020.113352 . hal-02957458

HAL Id: hal-02957458

<https://centralesupelec.hal.science/hal-02957458>

Submitted on 9 Dec 2020

HAL is a multi-disciplinary open access archive for the deposit and dissemination of scientific research documents, whether they are published or not. The documents may come from teaching and research institutions in France or abroad, or from public or private research centers.

L'archive ouverte pluridisciplinaire **HAL**, est destinée au dépôt et à la diffusion de documents scientifiques de niveau recherche, publiés ou non, émanant des établissements d'enseignement et de recherche français ou étrangers, des laboratoires publics ou privés.

Systematic development of upwind numerical fluxes for the space discontinuous Galerkin method applied to elastic wave propagation in anisotropic and heterogeneous media with physical interfaces

B. Tie^{a,*}, A.-S. Mouronval^a

^a*Université Paris-Saclay, CentraleSupélec, CNRS, Laboratoire de Mécanique des Sols, Structures et Matériaux (MSSMat-UMR8579), 91190, Gif-sur-Yvette, France.*

Abstract

This research work presents, within a unified and wave oriented variational framework, systematic development of upwind numerical fluxes for the space discontinuous Galerkin methods to model elastic wave propagation in multidimensional anisotropic media with discontinuous material properties. Both first-order velocity-stress and velocity-strain wave formulations are considered. The proposed approach allows the derivation of upwind numerical fluxes in a well structured and hierarchical way according to the degree of inhomogeneity across a physical interface. The numerical fluxes that are exact solutions of a relevant Riemann problem defined at a physical interface are obtained. The developed explicit and intrinsic tensorial expressions of upwind numerical fluxes in multidimensional case allow a better understanding and analysis of the physical meaning of involved terms. As numerical applications, an example with a physical interface separating two materials, one anisotropic and the other isotropic, and an example of polycrystalline material that presents a particular case with a larger number of physical interfaces, are considered. The proposed numerical fluxes are numerically investigated and validated.

Keywords: Space discontinuous Galerkin method; Elastic wave propagation, Anisotropy; Heterogeneous medium with physical interfaces; Polycrystalline materials

1. Introduction

2 The space discontinuous Galerkin (dG) method is based on the use of spa-
3 tially element-wise discontinuous finite element basis functions, and developing
4 appropriate numerical fluxes on element interfaces is a key point for its success

*Corresponding author

Email address: bing.tie@centralesupelec.fr (B. Tie)

5 [1, 2, 3, 4, 5, 6, 7, 8, 9, 10]. For this purpose, exact solving of the Riemann prob-
6 lem defined on element interfaces is usually recommended. However, when it is
7 applied to elastic media, upwind numerical fluxes solving exactly the Riemann
8 problem can be easily done only in the case of continuous material properties due
9 to the involvement of the fourth order elastic tensor. Recently, research work
10 has been proposed for the derivation of numerical fluxes at physical interfaces,
11 i.e., in the presence of material discontinuities, in 2D [7] or in 3D [6, 9, 10] cases.
12 All these works consider only the velocity-strain wave formulation for the elastic
13 media, and they are all placed in the multiphysics context coupling respectively,
14 isotropic elastic/acoustic media for Wilcox *et al.* [6], isotropic poroelastic/elastic
15 media for Ward *et al.* [7], anisotropic elastic media/fluid media for Zhan *et al.* [9],
16 or anisotropic poroelastic/elastic/fluid interfaces for Zhan *et al.* [10].

17 Besides, it is noteworthy that penalty fluxes, an alternative to upwind fluxes
18 for dG methods, have also been developed in the literature [11, 12, 13, 14]. To
19 derive numerical fluxes, the penalty method is energy stable and significantly less
20 complicated. The lack of dependence of penalty fluxes on the stiffness matrix
21 allows for a unified and efficient implementation [13]. However, by solving a
22 Riemann problem consistent with physical continuous interface conditions, an
23 upwind flux can be derived, and it is superior, *i.e.*, more accurate, to penalty
24 fluxes. Moreover, such an upwind flux is completely determined by the physical
25 problem itself, and there is no need to deal with the choice of a “numerical”
26 parameter as the penalty parameter for a penalty flux.

27 The aim of the present work is, by using the unified and wave oriented vari-
28 ational framework that we previously proposed in [8], to present a systematic
29 development of upwind numerical fluxes in the most general case of multidimen-
30 sional anisotropic elastic media with discontinuous material properties. Unlike
31 the above-cited works, both first-order velocity-stress formulation defined in
32 [2, 3, 5] and velocity-strain one defined in [6, 7, 9] of the elastic wave propaga-
33 tion are considered, and in both cases, closed-form expressions of exact solutions
34 of a Riemann problem defined at a physical interface are obtained. Owing to
35 compact and intrinsic forms expressed in terms of tensors, the derivation of
36 upwind numerical fluxes can be done in a well structured and hierarchical way,
37 which allows better understanding and analysis of the physical meaning of the
38 developed upwind numerical fluxes.

39 We note that, for the first-order velocity-strain formulation of elastic waves,
40 the numerical flux derived in the present work is the same as the one presented
41 in the above-cited works [7, 9]. Our contribution is a new method to derive the
42 upwind flux, using a coordinate-free vector and tensor notation, and exploiting
43 the elastic wave oriented eigenanalysis of a hyperbolic system. The formalism
44 proposed by Wilcox *et al.* [6] is close to ours, in the sense that the use of the
45 tensorial forms of strain and stress fields is preserved, but it is only developed
46 for the isotropic case and for the first-order velocity-strain formulation. While,
47 the formalism used in [7, 9, 10] is a “classical” one and is very different to ours,
48 because the strain and stress tensors are reformulated under a vector form.

49 As numerical applications, firstly, an example with a physical interface sep-
50 arating two materials, one anisotropic and the other isotropic, is studied. Then,

51 polycrystalline materials that present a particularly interesting case of hetero-
 52 geneous media with a very large number of physical interfaces are considered.
 53 Ultrasonic wave propagation in single-phase and untextured polycrystalline ma-
 54 terials composed of a large number of elliptic grains are simulated. The proposed
 55 numerical fluxes are numerically investigated and validated.

56 The paper is organized as follows. In Section 2, the unified variational frame-
 57 work using intrinsic tensorial expressions that was proposed in [8] is recalled for
 58 both first-order velocity-stress and velocity-strain hyperbolic systems of elas-
 59 tic wave equations. Section 3 presents the development of different upwind
 60 numerical fluxes for the first-order velocity-stress wave system. The necessity
 61 of defining a mechanically relevant Riemann problem at a physical interface is
 62 particularly discussed. Section 4 applies the proposed approach to the case of
 63 the first-order velocity-strain wave system. Finally, in Section 5, the proposed
 64 numerical fluxes are applied to the cases where one or more physical interfaces
 65 exist.

66 2. First-order elastic wave governing equations and their variational 67 frameworks

68 The governing equations of elastic wave propagation are firstly given in the
 69 form of a first-order velocity-stress system with velocity and stress field as pri-
 70 mary unknowns [2, 3, 4, 5] (see Eqs. (22.14–22.15) in [2]). Then, the uni-
 71 fied and wave oriented variational framework is introduced within which the
 72 eigen characteristics of the first-order hyperbolic system are presented and the
 73 variational discontinuous Galerkin formulation is given. Finally, the first-order
 74 velocity-strain wave equations used by Wilcox *et al.* [6] are also considered in
 75 the present work, as only isotropic media with physical interfaces were studied
 76 by those authors.

77 2.1. First-order velocity-stress elastic wave equations

78 We consider the wave propagation in an elastic medium $\Omega \subset \mathbb{R}^d$ of space
 79 dimension d ($d = 1, 2, 3$) and in a time interval $[0, T]$. The first-order velocity-
 80 stress governing equations can be written as follows: $\forall(\mathbf{x}, t) \in \Omega \times]0, T[$

$$\partial_t \mathbf{U} + \mathbf{A}^{\partial_x}(\mathbf{U}) = \mathbf{0} \quad \text{or} \quad \begin{aligned} \partial_t \mathbf{v} - \rho^{-1} \mathbf{Div}_x \boldsymbol{\sigma} &= \mathbf{0} \\ \partial_t \boldsymbol{\sigma} - \mathbf{C} : \boldsymbol{\varepsilon}(\mathbf{v}) &= \mathbf{0} \end{aligned} \quad (1)$$

81 The tensorial compact form in (1) has been proposed by the authors in [8]. The
 82 generalized unknown $\mathbf{U}(\mathbf{x}, t) = (\mathbf{v}(\mathbf{x}, t) \boldsymbol{\sigma}(\mathbf{x}, t))^T$ is composed of \mathbf{v} the velocity
 83 unknown and $\boldsymbol{\sigma}$ the stress unknown, with $(\cdot)^T$ the adjoint operator. Hence,
 84 $\mathbf{U}(\mathbf{x}, t)$ is a field in $\mathbb{R}^d \times \mathbb{R}^{d \times d_{sym}}$ and defined over the open set $\Omega \times]0, T[$, with
 85 $\mathbb{R}^{d \times d_{sym}}$ indicating that $\boldsymbol{\sigma}$ is a $d \times d$ symmetric second-order tensor. The partial
 86 derivative operator with respect to time is denoted ∂_t . The space derivative
 87 operator \mathbf{A}^{∂_x} and its adjoint $\mathbf{A}^{\partial_x, T}$ (useful hereafter) are defined as follows:
 88 $\forall \mathbf{W} = (\mathbf{w} \boldsymbol{\tau})^T$

$$\mathbf{A}^{\partial_x} \begin{pmatrix} \mathbf{w} \\ \boldsymbol{\tau} \end{pmatrix} = \begin{pmatrix} -\rho^{-1} \mathbf{Div}_x \boldsymbol{\tau} \\ -\mathbf{C} : \boldsymbol{\varepsilon}(\mathbf{w}) \end{pmatrix}, \quad \mathbf{A}^{\partial_x, T} \begin{pmatrix} \mathbf{w} \\ \boldsymbol{\tau} \end{pmatrix} = \begin{pmatrix} -\mathbf{Div}_x(\mathbf{C} : \boldsymbol{\tau}) \\ -\rho^{-1} \boldsymbol{\varepsilon}(\mathbf{w}) \end{pmatrix} \quad (2)$$

89 where ρ denotes the density, \mathbf{C} the fourth-order elasticity tensor, and “:” the
 90 usual double dot product between two tensors defined as $(\mathbf{C} : \boldsymbol{\varepsilon})_{ij} = C_{ijkl}\varepsilon_{kl}$.
 91 Herein, the Einstein summation convention is systematically used, and all the
 92 vectors and tensors are denoted using bold letters.

93 The two equations of (1) express respectively the elastodynamic equilibrium
 94 and the time derivative of the Hooke’s law of elasticity. No body force is con-
 95 sidered in the equilibrium equation without loss of generality of the purpose of
 96 the present work.

97 It is useful to recall that, according to the definition of the second-order
 98 infinitesimal strain tensor $\boldsymbol{\varepsilon}$, we have:

$$\boldsymbol{\varepsilon}(\mathbf{w}) = \frac{1}{2} \left(\mathbf{D}_x \mathbf{w} + \mathbf{D}_x^T \mathbf{w} \right) = \frac{\partial \mathbf{w}}{\partial x_i} \otimes_s \mathbf{e}_i \quad (3)$$

99 with the following usual space gradient and divergence operators defined using
 100 an orthonormal basis $(\mathbf{e}_i)_{i=1,\dots,d}$:

$$\mathbf{D}_x \mathbf{w} = \frac{\partial \mathbf{w}}{\partial x_i} \otimes \mathbf{e}_i, \quad \text{Div}_x \boldsymbol{\tau} = \frac{\partial \boldsymbol{\tau}}{\partial x_i} \cdot \mathbf{e}_i \quad (4)$$

101 In (4), “ \otimes ” denotes the usual tensor product between two vectors: $(\mathbf{a} \otimes \mathbf{b})_{ij} =$
 102 $a_i b_j$ and “ \cdot ” the usual dot product between a tensor and a vector: $(\mathbf{A} \cdot \mathbf{a})_i =$
 103 $A_{ij} a_j$. In (3), “ \otimes_s ” is the symmetrized tensor product defined as: $(\mathbf{a} \otimes_s \mathbf{b})_{ij} =$
 104 $\frac{1}{2}(a_i b_j + a_j b_i)$. Otherwise, it is useful to define the dot product in the vectorial
 105 space $\mathbb{R}^d \times \mathbb{R}^{d \times d_{sym}}$: $\forall \mathbf{W}_i = (\mathbf{w}_i \boldsymbol{\tau}_i)^T, (i = 1, 2)$,

$$\mathbf{W}_1 \cdot \mathbf{W}_2 = \mathbf{w}_1 \cdot \mathbf{w}_2 + \boldsymbol{\tau}_1 : \boldsymbol{\tau}_2 \quad (5)$$

106 According to (4), it is easy to show that, on the boundary ∂D of any subdomain
 107 $D \subseteq \Omega$, the flux operator \mathbf{F}_n (with $\mathbf{n} = n_i \mathbf{e}_i$ the outward unit normal vector
 108 defined on ∂D) associated to the first-order system (1) is in fact equal to \mathbf{A}_n ,
 109 the Jacobian operator in the \mathbf{n} direction: $\forall \mathbf{W} = (\mathbf{w} \boldsymbol{\tau})^T$,

$$\mathbf{F}_n(\mathbf{W}) = \mathbf{A}_n(\mathbf{W}) = \begin{pmatrix} -\rho^{-1} \boldsymbol{\tau} \cdot \mathbf{n} \\ -\mathbf{C} : (\mathbf{n} \otimes_s \mathbf{w}) \end{pmatrix} \quad (6)$$

110 In (6), the subscript index “ n ” indicates the dependency of \mathbf{F}_n and of \mathbf{A}_n on
 111 \mathbf{n} . In the following, the local orthonormal basis defined on $\partial\Omega$ will be denoted
 112 by $(\mathbf{n}, \{\mathbf{t}_\alpha\}_{\alpha=1,\dots,d-1})$.

Finally, to complete the definition of the elastic wave propagation problem,
 the following boundary conditions are prescribed:

$$\boldsymbol{\sigma} \cdot \mathbf{n} = \mathbf{g}, \quad \text{on } \partial\Omega_N \times]0, T[\quad (7a)$$

$$\mathbf{v} = \partial_t \mathbf{u}_D, \quad \text{on } \partial\Omega_D \times]0, T[\quad (7b)$$

The first equation (7a) expresses the Neumann boundary conditions with im-
 posed surface loadings \mathbf{g} , and the second one (7b) expresses the Dirichlet bound-
 ary conditions with prescribed displacements \mathbf{u}_D . We recall that the conditions

$\partial\Omega_N \cup \partial\Omega_D = \partial\Omega$ and $\partial\Omega_N \cap \partial\Omega_D = \emptyset$ should be verified. The following initial conditions are also necessary:

$$\boldsymbol{\sigma}(\mathbf{x}, 0) = \mathbf{C} : \boldsymbol{\varepsilon}(\mathbf{u}_0(\mathbf{x})), \quad \forall \mathbf{x} \in \Omega \quad (8a)$$

$$\mathbf{v}(\mathbf{x}, 0) = \mathbf{v}_0(\mathbf{x}), \quad \forall \mathbf{x} \in \Omega \quad (8b)$$

113 To develop the variational framework for the space dG method, we recall
 114 that an approximated solution $\mathbf{U}_h = (\mathbf{v}_h \ \boldsymbol{\sigma}_h)^T$ of the generalized unknown
 115 $\mathbf{U} = (\mathbf{v} \ \boldsymbol{\sigma})^T$ is sought for, and, in contrast to continuous finite element methods,
 116 \mathbf{U}_h is discontinuous from one element to another.

Let $\mathcal{M}_h = \{\Omega_k\}_k$ denote a finite element mesh of Ω . In the following, any element Ω_k of the mesh \mathcal{M}_h will be denoted by E and any of its neighboring elements by E' . The discontinuous solutions in E and E' are respectively denoted by \mathbf{U}_h and \mathbf{U}'_h . Then, the space dG variational formulation of the elastic wave model problem (1) for any element E can be put into two equivalent forms:
 $\forall \mathbf{W}_h(\mathbf{x}) = (\mathbf{w}_h(\mathbf{x}) \ \boldsymbol{\tau}_h(\mathbf{x}))^T$

$$(\mathbf{W}_h, \partial_t \mathbf{U}_h)_E - (\mathbf{A}^{\partial_x, T}(\mathbf{W}_h), \mathbf{U}_h)_{E+} + \langle \mathbf{W}_h, \hat{\mathbf{F}}_n(\mathbf{U}_h, \mathbf{U}'_h) \rangle_{\partial E} = 0 \quad (9a)$$

$$(\mathbf{W}_h, \partial_t \mathbf{U}_h)_E + (\mathbf{W}_h, \mathbf{A}^{\partial_x}(\mathbf{U}_h))_{E+} + \langle \mathbf{W}_h, \hat{\mathbf{F}}_n(\mathbf{U}_h, \mathbf{U}'_h) - \mathbf{F}_n(\mathbf{U}_h) \rangle_{\partial E} = 0 \quad (9b)$$

117 In (9), the inner products are defined as follows by recalling the definition of
 118 the dot product given in (5):

$$\begin{aligned} (\mathbf{w}_1, \mathbf{w}_2)_E &= \int_E \mathbf{w}_1 \cdot \mathbf{w}_2 \, dV, (\boldsymbol{\tau}_1, \boldsymbol{\tau}_2)_E = \int_E \boldsymbol{\tau}_1 : \boldsymbol{\tau}_2 \, dV \\ (\mathbf{W}_1, \mathbf{W}_2)_E &= \int_E \mathbf{W}_1 \cdot \mathbf{W}_2 \, dV = (\mathbf{w}_1, \mathbf{w}_2)_E + (\boldsymbol{\tau}_1, \boldsymbol{\tau}_2)_E \end{aligned} \quad (10)$$

119 One of the basic ideas of the space dG method is to replace the discontinuous
 120 flux $\mathbf{F}_n(\mathbf{U}_h)$ on the element boundary ∂E by a numerical flux $\hat{\mathbf{F}}_n(\mathbf{U}_h, \mathbf{U}'_h)$.
 121 Hence, an appropriate choice of the numerical flux is essential for the success of
 122 the space dG method. Only the definition of the numerical flux on the interior
 123 element boundary $\partial E_{int} = \partial E \setminus (\partial E \cap \partial\Omega)$, which should also depend on the
 124 solution \mathbf{U}'_h in the neighboring elements E' of E , is studied in the present work.

125 As for the numerical flux on external element boundary $\partial E_{ext} = \partial E \cap$
 126 $\partial\Omega$, a ghost neighbor element E' having the same mechanical behavior as E
 127 is introduced [2]. In E' , it should be imposed that: $\boldsymbol{\sigma}'_h \cdot \mathbf{n} = 2\mathbf{g} - \boldsymbol{\sigma}_h \cdot \mathbf{n}$ and
 128 $\mathbf{v}'_h = \mathbf{v}_h$ for the Neumann boundary conditions on $\partial\Omega_N$, and $\boldsymbol{\sigma}'_h \cdot \mathbf{n} = \boldsymbol{\sigma}_h \cdot \mathbf{n}$
 129 and $\mathbf{v}'_h = 2\partial_t \mathbf{u}_D - \mathbf{v}_h$ for the Dirichlet boundary conditions on $\partial\Omega_D$.

130 Otherwise, we have chosen in our numerical studies to implement the second
 131 variational dG formulation (9b), because the terms involved in the differential
 132 operator \mathbf{A}^{∂_x} are slightly more conventional than those involved in the differ-
 133 ential operator $\mathbf{A}^{\partial_x, T}$, which is invoked by (9a).

134 2.2. First-order velocity-strain elastic wave equations

135 For the first-order velocity-strain wave equations used in [6], the generalized
 136 unknown $\mathbf{U}(\mathbf{x}, t) = (\mathbf{v}(\mathbf{x}, t) \ \boldsymbol{\varepsilon}(\mathbf{x}, t))^T$ is composed of \mathbf{v} the velocity unknown

137 and $\boldsymbol{\varepsilon}$ the strain unknown. The corresponding tensorial compact form can be
 138 written as follows: $\forall(\boldsymbol{x}, t) \in \Omega \times]0, T[$

$$M(\partial_t \boldsymbol{U}) + \boldsymbol{A}^{\partial_x}(\boldsymbol{U}) = \mathbf{0} \quad \text{or} \quad \begin{aligned} \rho \partial_t \boldsymbol{v} - \text{Div}_x(\boldsymbol{C} : \boldsymbol{\varepsilon}) &= \mathbf{0} \\ \partial_t \boldsymbol{\varepsilon} - \boldsymbol{C} : \boldsymbol{\varepsilon}(\boldsymbol{v}) &= \mathbf{0} \end{aligned} \quad (11)$$

139 In (11), the infinitesimal strain operator $\boldsymbol{\varepsilon}(\cdot)$ defined by (3) should be distin-
 140 guished from the primary unknown $\boldsymbol{\varepsilon} = \boldsymbol{\varepsilon}(\boldsymbol{x}, t)$. The operator \boldsymbol{M} and the space
 141 derivative operator $\boldsymbol{A}^{\partial_x}$ are defined as follows: $\forall \boldsymbol{W} = (\boldsymbol{w} \ \boldsymbol{\tau})^T$

$$\boldsymbol{M} \begin{pmatrix} \boldsymbol{w} \\ \boldsymbol{\tau} \end{pmatrix} = \begin{pmatrix} \rho \boldsymbol{w} \\ \boldsymbol{\tau} \end{pmatrix}, \quad \boldsymbol{A}^{\partial_x} \begin{pmatrix} \boldsymbol{w} \\ \boldsymbol{\tau} \end{pmatrix} = \begin{pmatrix} -\text{Div}_x(\boldsymbol{C} : \boldsymbol{\tau}) \\ -\boldsymbol{\varepsilon}(\boldsymbol{w}) \end{pmatrix} \quad (12)$$

142 Then, the flux operator \boldsymbol{F}_n associated to the first-order system (11) and
 143 the Jacobian operator \boldsymbol{A}_n in the \boldsymbol{n} direction verify the following equations:
 144 $\forall \boldsymbol{W} = (\boldsymbol{w} \ \boldsymbol{\tau})^T$,

$$\boldsymbol{F}_n(\boldsymbol{W}) = \boldsymbol{A}_n(\boldsymbol{W}) = \begin{pmatrix} -(\boldsymbol{C} : \boldsymbol{\tau}) \cdot \boldsymbol{n} \\ -\boldsymbol{n} \otimes_s \boldsymbol{w} \end{pmatrix} \quad (13)$$

145 The corresponding variational framework reads as:

$$(\boldsymbol{W}_h, \boldsymbol{M}(\partial_t \boldsymbol{U}_h))_{E^+} + (\boldsymbol{W}_h, \boldsymbol{A}^{\partial_x}(\boldsymbol{U}_h))_{E^+} + \langle \boldsymbol{W}_h, \hat{\boldsymbol{F}}_n(\boldsymbol{U}_h, \boldsymbol{U}'_h) - \boldsymbol{F}_n(\boldsymbol{U}_h) \rangle_{\partial E} = 0 \quad (14)$$

146 It is worth noticing that the same notations are used in this paper for both
 147 velocity-stress and velocity-strain systems but may have different definitions.

148 3. Upwind numerical fluxes for the 1st-order velocity-stress system

149 In this section, upwind numerical fluxes are firstly developed for the first-
 150 order velocity-stress wave equations. It is emphasized that the unified and
 151 elastic wave oriented variational framework previously proposed in [8] allows a
 152 simple, compact and intrinsic expression of the Jacobian operator of the first-
 153 order hyperbolic system (1) in terms of its eigenvalues and eigenmodes. As a
 154 consequence, a systematic development of numerical fluxes can be formulated
 155 in the multidimensional and general case, *i.e.* anisotropic and heterogeneous
 156 media with physical interfaces. Moreover, it allows a better understanding of
 157 the physical meaning of the terms involved in the developed numerical fluxes.

158 Before giving the definition of the Riemann problem on element interfaces,
 159 it is useful to recall some important results given in [8].

160 First, the normal Jacobian operator \boldsymbol{A}_n (defined by (6)) of the first-order
 161 velocity-stress wave equations (1) can be decomposed as follows, using its two
 162 eigenbases:

$$\boldsymbol{A}_n = \lambda_{\boldsymbol{n},k}^- \boldsymbol{R}_{\boldsymbol{n},k}^- \otimes \boldsymbol{L}_{\boldsymbol{n},k}^- + \lambda_{\boldsymbol{n},k}^+ \boldsymbol{R}_{\boldsymbol{n},k}^+ \otimes \boldsymbol{L}_{\boldsymbol{n},k}^+ \quad (15)$$

163 where $(\lambda_{\boldsymbol{n},k}^-, \boldsymbol{R}_{\boldsymbol{n},k}^-, \boldsymbol{L}_{\boldsymbol{n},k}^-)_{k=qL, \{qT_\alpha\}_{\alpha=1, d-1}}$ and $(\lambda_{\boldsymbol{n},k}^+, \boldsymbol{R}_{\boldsymbol{n},k}^+, \boldsymbol{L}_{\boldsymbol{n},k}^+)_{k=qL, \{qT_\alpha\}_{\alpha=1, d-1}}$
 164 are respectively the strictly negative and positive eigenvalues and the corre-
 165 sponding right and left eigenvectors of \boldsymbol{A}_n . The left eigenvectors are the eigen-
 166 vectors of the adjoint of \boldsymbol{A}_n .

167 As a matter of fact, among the $m = d + d(d + 1)/2$ eigenvalues of \mathbf{A}_n ,
 168 there are d strictly negative eigenvalues $(\lambda_{n,k}^- = -c_{n,k})_{k=qL, \{qT_\alpha\}_{\alpha=1, \dots, d-1}}$ and
 169 d strictly positive eigenvalues $(\lambda_{n,k}^+ = c_{n,k})_{k=qL, \{qT_\alpha\}_{\alpha=1, \dots, d-1}}$, $c_{n,qL}$ and c_{n,qT_α}
 170 being respectively the velocity of quasi longitudinal and quasi transverse wave
 171 modes propagating in the \mathbf{n} direction. The subscript indices “ qL ” and “ qT ”
 172 respectively refer to terms “quasi longitudinal” and “quasi transverse”.

173 Then, it has been shown that the right and left eigenmodes corresponding
 174 to the nonzero eigenvalues of \mathbf{A}_n are the following: $\forall k = qL, \{qT_\alpha\}_{\alpha=1, \dots, d-1}$

$$R_{n,k}^\pm = \begin{pmatrix} \mathbf{w}_{n,k} \\ -\rho(z_{n,k}^\pm)^{-1} \mathbf{C} : (\mathbf{n} \otimes_s \mathbf{w}_{n,k}) \end{pmatrix}, \quad L_{n,k}^\pm = \begin{pmatrix} \mathbf{w}_{n,k} \\ -(z_{n,k}^\pm)^{-1} \mathbf{n} \otimes_s \mathbf{w}_{n,k} \end{pmatrix} \quad (16)$$

175 with $z_{n,k}^\pm = \rho \lambda_{n,k}^\pm$ the acoustic impedance, $\mathbf{w}_{n,k} = \frac{1}{\sqrt{2}} \boldsymbol{\gamma}_{n,k}$, $(\boldsymbol{\gamma}_{n,k})_{k=qL, \{qT_\alpha\}_{\alpha=1, \dots, d-1}}$
 176 the unit eigenvectors of the following usual eigensystem of $\boldsymbol{\Gamma}_n$ the Christoffel
 177 tensor:

$$\boldsymbol{\Gamma}_n \cdot \boldsymbol{\gamma}_{n,k} = \lambda_{n,k}^2 \boldsymbol{\gamma}_{n,k} \quad (17)$$

178 The definition of the Christoffel tensor $\boldsymbol{\Gamma}_n$ is recalled in the following:

$$\boldsymbol{\Gamma}_n \cdot \mathbf{w} = \rho^{-1} (\mathbf{C} : (\mathbf{n} \otimes_s \mathbf{w})) \cdot \mathbf{n}, \quad \forall \mathbf{w} \quad (18)$$

179 For instance, in the 3D case, there are one quasi longitudinal wave mode
 180 and two quasi transverse wave modes. We recall that the word “quasi” means
 181 that, in contrast to the isotropic case, we have in the general anisotropic case
 182 neither pure longitudinal wave mode verifying $\boldsymbol{\gamma}_{n,qL} \parallel \mathbf{n}$ nor pure transverse
 183 waves modes verifying $\boldsymbol{\gamma}_{n,qT} \perp \mathbf{n}$.

184 Furthermore, we note that the right and left eigenmodes corresponding to
 185 the zero eigenvalues of \mathbf{A}_n are not recalled herein, as they are not involved
 186 in the decomposition of \mathbf{A}_n (15) and therefore are not involved in flux terms
 187 exchanged on element interfaces.

188 Among existing works, the numerical flux proposed in [3, 4] uses the same
 189 velocity-stress formulation (1), but it is only an approximate solution of the Rie-
 190 mann problem defined on a physical interface across which material properties
 191 are discontinuous. However, we have shown in [8] that, when a numerical flux is
 192 not the exact solution of the Riemann problem, it works only when the degree
 193 of discontinuity across the physical interface is low. Hereafter, a systematic de-
 194 velopment of upwind numerical fluxes that are exact solutions of the Riemann
 195 problem in the multidimensional case, *i.e.* 2D and 3D, is proposed.

196 Otherwise, another important result we have shown in the 1D case is that
 197 solving exactly the Riemann problem at element interfaces is not a sufficient con-
 198 dition to get physically sound numerical solutions [8]. Indeed, different equiv-
 199 alent strong forms of the elastic wave problem give rise to different forms of
 200 the Riemann problem and consequently to different interface conditions, which
 201 are not all physically coherent. To perform the same analysis in the multid-
 202 imensional case, two upwind numerical fluxes are developed in the following:
 203 the first one is the solution of the Riemann problem directly defined from the
 204 first-order velocity-stress system (1), while the second one is the solution of

205 the Riemann problem modified by taking into account the classical mechanical
 206 interface conditions in terms of velocity and stress vector fields.

207 *3.1. Upwind flux directly derived from the first-order \mathbf{v} - $\boldsymbol{\sigma}$ system (1)*

208 We consider the interface of two adjacent elements E and E' having respec-
 209 tively $(\rho, \mathbf{C}, \mathbf{U}_h)$ and $(\rho', \mathbf{C}', \mathbf{U}'_h)$ as densities, elastic moduli and initial states
 210 (Figure 1). The Riemann problem defines the states that are results of the
 211 propagation of the discontinuity $\mathbf{U}_h - \mathbf{U}'_h$. In the following, all the equations
 are written in the 3D case without loss of generality.

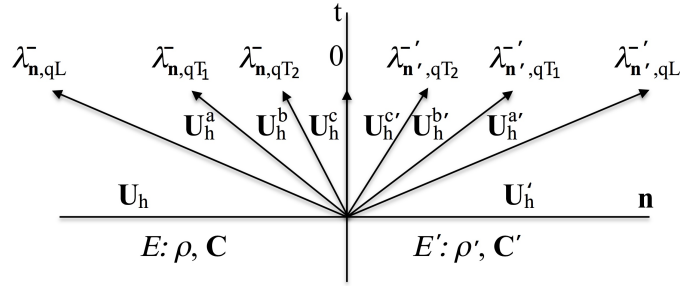


Figure 1: Sketch illustrating the Rankine-Hugoniot jump conditions in the Riemann problem in the 3D case.

212

In the 3D anisotropic case and by assuming $\lambda_{\mathbf{n},qL}^- < \lambda_{\mathbf{n},qT1}^- < \lambda_{\mathbf{n},qT2}^-$, the Rankine-Hugoniot jump conditions for the first-order velocity-stress system (1) are illustrated in Figure 1 and read as [2, 8, 6, 15]:

$$\mathbf{A}_{\mathbf{n}}(\mathbf{U}_h - \mathbf{U}_h^a) = \lambda_{\mathbf{n},qL}^-(\mathbf{U}_h - \mathbf{U}_h^a) \quad (19a)$$

$$\mathbf{A}_{\mathbf{n}}(\mathbf{U}_h^a - \mathbf{U}_h^b) = \lambda_{\mathbf{n},qT1}^-(\mathbf{U}_h^a - \mathbf{U}_h^b), \mathbf{A}_{\mathbf{n}}(\mathbf{U}_h^b - \mathbf{U}_h^c) = \lambda_{\mathbf{n},qT2}^-(\mathbf{U}_h^b - \mathbf{U}_h^c) \quad (19b)$$

$$\mathbf{A}_{\mathbf{n}} \cdot \mathbf{U}_h^c + \mathbf{A}'_{\mathbf{n}'} \cdot \mathbf{U}_h^{c'} = \mathbf{0} \quad (19c)$$

$$\mathbf{A}'_{\mathbf{n}'}(\mathbf{U}_h^{b'} - \mathbf{U}_h^{c'}) = \lambda_{\mathbf{n}',qT2}^-(\mathbf{U}_h^{b'} - \mathbf{U}_h^{c'}), \mathbf{A}'_{\mathbf{n}'}(\mathbf{U}_h^{a'} - \mathbf{U}_h^{b'}) = \lambda_{\mathbf{n}',qT1}^-(\mathbf{U}_h^{a'} - \mathbf{U}_h^{b'}) \quad (19d)$$

$$\mathbf{A}'_{\mathbf{n}'}(\mathbf{U}'_h - \mathbf{U}_h^{a'}) = \lambda_{\mathbf{n},qL}^-(\mathbf{U}'_h - \mathbf{U}_h^{a'}) \quad (19e)$$

We note that the two outward unit normal vectors of E and E' on their interface verify $\mathbf{n} + \mathbf{n}' = \mathbf{0}$. According to the definition of the eigenvalues and eigenvectors

of \mathbf{A}_n , the following equations hold:

$$\mathbf{U}_h - \mathbf{U}_h^a = \alpha_{qL} \mathbf{R}_{n,qL}^-, \mathbf{U}_h^a - \mathbf{U}_h^b = \alpha_{qT_1} \mathbf{R}_{n,qT_1}^-, \mathbf{U}_h^b - \mathbf{U}_h^c = \alpha_{qT_2} \mathbf{R}_{n,qT_2}^- \quad (20a)$$

$$\mathbf{U}_h' - \mathbf{U}_h^{a'} = \alpha'_{qL} \mathbf{R}_{n',qL}^-, \mathbf{U}_h^{a'} - \mathbf{U}_h^{b'} = \alpha'_{qT_1} \mathbf{R}_{n',qT_1}^-, \mathbf{U}_h^{b'} - \mathbf{U}_h^{c'} = \alpha'_{qT_2} \mathbf{R}_{n',qT_2}^- \quad (20b)$$

By respectively adding the three first equations given by (19a)–(19b) and the three last equations given by (19d)–(19e) and by applying (20), the Rankine–Hugoniot jump conditions finally become:

$$\mathbf{A}_n(\mathbf{U}_h) - \mathbf{A}_n(\mathbf{U}_h^c) = \alpha_k \lambda_{n,k}^- \mathbf{R}_{n,k}^- \quad (21a)$$

$$\mathbf{A}_n(\mathbf{U}_h^c) + \mathbf{A}'_{n'}(\mathbf{U}_h^{c'}) = \mathbf{0} \quad (21b)$$

$$\mathbf{A}'_{n'}(\mathbf{U}_h') - \mathbf{A}'_{n'}(\mathbf{U}_h^{c'}) = \alpha'_k \lambda_{n',k}^- \mathbf{R}_{n',k}^- \quad (21c)$$

In the case where $\lambda_{n,qT_1}^- = \lambda_{n,qT_2}^-$ (resp. $\lambda_{n',qT_1}^- = \lambda_{n',qT_2}^-$), the two arrows λ_{n,qT_1}^- and λ_{n,qT_2}^- (resp. λ_{n',qT_1}^- and λ_{n',qT_2}^-) in Figure 1 overlap, and the state \mathbf{U}_h^b (resp. $\mathbf{U}_h^{b'}$) is removed. Then, the equations (19b) and (20a) become:

$$\mathbf{A}_n(\mathbf{U}_h^a - \mathbf{U}_h^c) = \lambda_{n,qT_1}^- (\mathbf{U}_h^a - \mathbf{U}_h^c) \quad (22a)$$

$$\mathbf{U}_h - \mathbf{U}_h^a = \alpha_{qL} \mathbf{R}_{n,qL}^-, \mathbf{U}_h^a - \mathbf{U}_h^c = \alpha_{qT_1} \mathbf{R}_{n,qT_1}^- + \alpha_{qT_2} \mathbf{R}_{n,qT_2}^- \quad (22b)$$

213 which finally lead to the same Rankine–Hugoniot jump conditions (21a). Same
214 remark holds for the quantities related to the element E' and the corresponding
215 equations (19d), (20b) and (21c).

Solving the Riemann problem (21) leads to the determination of the six unknown states $\{\mathbf{U}^a, \mathbf{U}^b, \mathbf{U}^c, \mathbf{U}^{a'}, \mathbf{U}^{b'}, \mathbf{U}^{c'}\}$, *i.e.*, the six characteristic coefficients $\{\alpha_k, \alpha'_k\}_{k=qL,qT_1,qT_2}$. Then, upwind numerical fluxes defined as $\hat{\mathbf{F}}_n(\mathbf{U}_h, \mathbf{U}_h') = \mathbf{A}_n(\mathbf{U}_h^c) = \frac{1}{2}(\mathbf{A}_n(\mathbf{U}_h^c) - \mathbf{A}'_{n'}(\mathbf{U}_h^{c'}))$ can be calculated by using the following two equivalent forms:

$$\hat{\mathbf{F}}_n(\mathbf{U}_h, \mathbf{U}_h') = \frac{1}{2}(\mathbf{A}_n(\mathbf{U}_h) - \mathbf{A}'_{n'}(\mathbf{U}_h') - \alpha_k \lambda_{n,k}^- \mathbf{R}_{n,k}^- + \alpha'_k \lambda_{n',k}^- \mathbf{R}_{n',k}^-) \quad (23a)$$

$$= \mathbf{A}_n(\mathbf{U}_h) - \alpha_k \lambda_{n,k}^- \mathbf{R}_{n,k}^- \quad (23b)$$

216 It is worth noticing that the two forms (23a) and (23b) are equivalent only in the
217 case where the Riemann problem (21) is exactly solved. Otherwise, according
218 to (21b), the flux defined by (23) is conservative, *i.e.*, from the point of view of
219 the neighboring element E' , we have $\hat{\mathbf{F}}_{n'}(\mathbf{U}_h', \mathbf{U}_h) = -\hat{\mathbf{F}}_n(\mathbf{U}_h, \mathbf{U}_h')$.

220 Now, the solving of the Riemann problem is considered. Two operators
221 $\wp_{vect}(\cdot)$ and $\wp_{tens}(\cdot)$ are defined: when applied to a generalized vector $\mathbf{W} =$
222 $(\mathbf{w} \ \boldsymbol{\tau})^T$, they respectively give its vectorial and tensorial components:

$$\wp_{vect}(\mathbf{W}) = \mathbf{w} \ , \ \wp_{tens}(\mathbf{W}) = \boldsymbol{\tau} \quad (24)$$

223 Using \wp_{vect} and \wp_{tens} , the vectorial part and the tensorial parts of the equa-
 224 tions (21b) can be separately manipulated. According to the definition of the
 225 Jacobian operator (6) and the definition (18) of the Christoffel tensor $\Gamma_{\mathbf{n}}$, (21b)
 226 is rewritten as follows:

$$\frac{\sigma_h^c \cdot \mathbf{n}}{\rho} + \frac{\sigma_h^{c'} \cdot \mathbf{n}'}{\rho'} = \mathbf{0}, \quad \rho \Gamma_{\mathbf{n}} \cdot \mathbf{v}_h^c - \rho' \Gamma_{\mathbf{n}'} \cdot \mathbf{v}_h^{c'} = \mathbf{0} \quad (25)$$

227 The second equation of (25) is obtained by applying the operator $\mathbf{n} \cdot \wp_{tens}$ to
 228 Eq.(21b).

229 Then, by eliminating the two unknown states U_h^c and $U_h^{c'}$ in (21) and using
 230 (25), the following result is obtained.

231 **Theorem 3.1.** *The characteristic coefficients $\{\alpha_k, \alpha'_k\}_{k=qL, qT_1, qT_2}$ of the Rie-*
 232 *mann problem (21) are the solution of the following system of linear equations:*

$$\begin{bmatrix} [I_d] & [B] \\ [B'] & [I_d] \end{bmatrix} \cdot \begin{pmatrix} \{\alpha_k\} \\ \{\alpha'_k\} \end{pmatrix} = \begin{pmatrix} \{*\mathbf{L}_{\mathbf{n},k}^- \cdot \mathbf{U}_h - **\mathbf{L}_{\mathbf{n},k}^- \cdot \mathbf{U}_h'\} \\ \{*\mathbf{L}_{\mathbf{n}',k}^- \cdot \mathbf{U}_h' - **\mathbf{L}_{\mathbf{n}',k}^- \cdot \mathbf{U}_h\} \end{pmatrix} \quad (26)$$

234 In (26), $[I_d]$ is the $d \times d$ identity matrix, and $[B]$ and $[B']$ are $d \times d$ matrices
 235 with zero diagonal terms and the following extra-diagonal terms:

$$B_{kl, k \neq l} = \frac{C_{z,k}^-}{2} \frac{\rho}{\rho'} \frac{z_{\mathbf{n}',l}^- \delta z_{\mathbf{n}',kl}^-}{z_{\mathbf{n},k}^- z_{\mathbf{n}',k}^-} \gamma_{\mathbf{n},k} \cdot \gamma_{\mathbf{n}',l}', \quad B'_{kl, k \neq l} = \frac{C_{z,k}^-}{2} \frac{\rho'}{\rho} \frac{z_{\mathbf{n},l}^- \delta z_{\mathbf{n},kl}^-}{z_{\mathbf{n}',k}^- z_{\mathbf{n},k}^-} \gamma_{\mathbf{n}',k}' \cdot \gamma_{\mathbf{n},l} \quad (27)$$

236 with $\delta z_{\mathbf{n},kl}^- = z_{\mathbf{n},k}^- - z_{\mathbf{n},l}^-$, $\delta z_{\mathbf{n}',kl}^- = z_{\mathbf{n}',k}^- - z_{\mathbf{n}',l}^-$, and :

$$C_{z,k}^- = \frac{\overline{\overline{z_{\mathbf{n},k}^-}}^R}{z_{\mathbf{n},k}^-} = \frac{z_{\mathbf{n},k}^-}{\overline{\overline{z_{\mathbf{n},k}^-}}^V} > 0, \quad C_{z,k}' = \frac{\overline{\overline{z_{\mathbf{n},k}^-}}^R}{z_{\mathbf{n}',k}^-} = \frac{z_{\mathbf{n},k}^-}{\overline{\overline{z_{\mathbf{n},k}^-}}^V} > 0 \quad (28)$$

237 $\overline{\overline{z_{\mathbf{n},k}^-}}^R$ and $\overline{\overline{z_{\mathbf{n},k}^-}}^V$ respectively denote the harmonic and arithmetic means of the
 238 acoustic impedances of the k -th eigenvector. $\{*\mathbf{L}_{\mathbf{n},k}^-, **\mathbf{L}_{\mathbf{n},k}^-, *\mathbf{L}_{\mathbf{n}',k}^-, **\mathbf{L}_{\mathbf{n}',k}^-\}$ are
 239 the perturbed left eigenmodes of $\{\mathbf{A}_{\mathbf{n}}, \mathbf{A}'_{\mathbf{n}'}\}$ calculated by using the material prop-
 240 erties of the adjacent element in the following way:

$$\begin{aligned} *\mathbf{L}_{\mathbf{n},k}^- &= \begin{pmatrix} C_{z,k}^- \wp_{vect}(\mathbf{L}_{\mathbf{n},k}^-) \\ C_{z,k}^- \wp_{tens}(\mathbf{L}_{\mathbf{n},k}^-) \end{pmatrix}, \quad **\mathbf{L}_{\mathbf{n},k}^- = \begin{pmatrix} \frac{\rho \rho'}{(z_{\mathbf{n},k}^-)^2} \Gamma_{\mathbf{n}'} \cdot \wp_{vect}(*\mathbf{L}_{\mathbf{n},k}^-) \\ \frac{\rho}{\rho'} \wp_{tens}(*\mathbf{L}_{\mathbf{n},k}^-) \end{pmatrix} \\ *\mathbf{L}_{\mathbf{n}',k}^- &= \begin{pmatrix} C_{z,k}^- \wp_{vect}(\mathbf{L}_{\mathbf{n}',k}^-) \\ C_{z,k}^- \wp_{tens}(\mathbf{L}_{\mathbf{n}',k}^-) \end{pmatrix}, \quad **\mathbf{L}_{\mathbf{n}',k}^- = \begin{pmatrix} \frac{\rho' \rho}{(z_{\mathbf{n}',k}^-)^2} \Gamma_{\mathbf{n}} \cdot \wp_{vect}(*\mathbf{L}_{\mathbf{n}',k}^-) \\ \frac{\rho'}{\rho} \wp_{tens}(*\mathbf{L}_{\mathbf{n}',k}^-) \end{pmatrix} \end{aligned} \quad (29)$$

241 *Proof.* See Appendix A1. □

242

243 It is worth noticing that the perturbed left eigenmodes $\{*\mathbf{L}_{\mathbf{n},k}^-, **\mathbf{L}_{\mathbf{n},k}^-\}$ and
 244 $\{*\mathbf{L}_{\mathbf{n}',k}^-, **\mathbf{L}_{\mathbf{n}',k}^-\}$ take into account the coupling between the wave modes of the
 245 same type, *e.g.*, both qL -modes, of the adjacent elements E and E' . In contrast,
 246 the matrices $[B]$ and $[B']$ take into account the coupling between two wave modes
 247 of different types, *e.g.*, a qL wave mode from E with a qT wave mode from E' .
 248 We also remark that (27) and (29) are completely symmetric with respect to E
 249 and E' .

250 Before giving one of the main results of the present work, it is worth recalling
 251 the numerical flux proposed by Käser *et al.* [3], which is expressed only in terms
 252 of material properties from the interior of the element E from one side of element
 253 interface, *i.e.*,

$$\hat{\mathbf{F}}_{\mathbf{n}}^{\text{Käser}}(\mathbf{U}_h, \mathbf{U}'_h) = \lambda_{\mathbf{n},k}^+(\mathbf{R}_{\mathbf{n},k}^+ \otimes \mathbf{L}_{\mathbf{n},k}^+) \cdot \mathbf{U}_h + \lambda_{\mathbf{n},k}^-(\mathbf{R}_{\mathbf{n},k}^- \otimes \mathbf{L}_{\mathbf{n},k}^-) \cdot \mathbf{U}'_h \quad (30)$$

254 Indeed, it would be interesting to present new terms brought by the upwind
 255 numerical fluxes proposed in the present work.

256 To obtain the upwind numerical fluxes, the linear system (26) needs to be
 257 solved. The $2d \times 2d$ matrix of the system of (26) denoted hereafter by $[R]$ will
 258 be decomposed into two parts: $[R] = [I_{2d}] + [\Delta R]$. Then the following upwind
 259 numerical fluxes are proposed:

260 **Theorem 3.2.** *According to how the inverse of $[R]$ the matrix of the system of*
 261 *(26) is approached, three upwind numerical fluxes can be defined as follows:*

262 1) *1st-order upwind numerical flux by taking $[R]^{-1} \approx [I_{2d}]$ and by remarking*
 263 *that $[R] \cdot [I_{2d}] - [I_{2d}] = [\Delta R]$*

$$\begin{aligned} \hat{\mathbf{F}}_{\mathbf{n}}(\mathbf{U}_h, \mathbf{U}'_h) &= \hat{\mathbf{F}}_{\mathbf{n}}^{\text{Käser}}(\mathbf{U}_h, \mathbf{U}'_h) \\ &+ \lambda_{\mathbf{n},k}^- ((\mathbf{R}_{\mathbf{n},k}^- \otimes (\mathbf{L}_{\mathbf{n},k}^- - *\mathbf{L}_{\mathbf{n},k}^-)) \cdot \mathbf{U}_h - (\mathbf{R}_{\mathbf{n},k}^- \otimes (\mathbf{L}_{\mathbf{n},k}^- - **\mathbf{L}_{\mathbf{n},k}^-)) \cdot \mathbf{U}'_h) \end{aligned} \quad (31)$$

264 2) *2nd-order upwind numerical flux by taking $[R]^{-1} \approx [I_{2d}] - [\Delta R]$ and by*
 265 *remarking that $[R] \cdot ([I_{2d}] - [\Delta R]) - [I_{2d}] = [\Delta R]^2$*

$$\begin{aligned} \hat{\mathbf{F}}_{\mathbf{n}}(\mathbf{U}_h, \mathbf{U}'_h) &= \hat{\mathbf{F}}_{\mathbf{n}}^{\text{1st-order}}(\mathbf{U}_h, \mathbf{U}'_h) \\ &- \lambda_{\mathbf{n},k}^- \sum_{l \neq k} B_{kl} ((\mathbf{R}_{\mathbf{n},k}^- \otimes **\mathbf{L}_{\mathbf{n}',l}^-) \cdot \mathbf{U}_h - (\mathbf{R}_{\mathbf{n},k}^- \otimes *\mathbf{L}_{\mathbf{n}',l}^-) \cdot \mathbf{U}'_h) \end{aligned} \quad (32)$$

266 where $\hat{\mathbf{F}}_{\mathbf{n}}^{\text{1st-order}}(\mathbf{U}_h, \mathbf{U}'_h)$ denotes the flux defined by (31).

267 3) *Upwind numerical flux being the exact solution of the Riemann problem(21)*

$$\begin{aligned} \hat{\mathbf{F}}_{\mathbf{n}}(\mathbf{U}_h, \mathbf{U}'_h) &= \hat{\mathbf{F}}_{\mathbf{n}}^{\text{1st-order}}(\mathbf{U}_h, \mathbf{U}'_h) \\ &- \lambda_{\mathbf{n},k}^- D_{kl} ((\mathbf{R}_{\mathbf{n},k}^- \otimes *\mathbf{L}_{\mathbf{n},l}^-) \cdot \mathbf{U}_h - (\mathbf{R}_{\mathbf{n},k}^- \otimes **\mathbf{L}_{\mathbf{n},l}^-) \cdot \mathbf{U}'_h) \\ &- \lambda_{\mathbf{n},k}^- H_{kl} ((\mathbf{R}_{\mathbf{n},k}^- \otimes **\mathbf{L}_{\mathbf{n}',l}^-) \cdot \mathbf{U}_h - (\mathbf{R}_{\mathbf{n},k}^- \otimes *\mathbf{L}_{\mathbf{n}',l}^-) \cdot \mathbf{U}'_h) \end{aligned} \quad (33)$$

268 with $[D]$, $[D']$, $[H]$ and $[H']$ four $d \times d$ matrices defined by the following decom-
 269 position of the inverse matrix of $[R]$:

$$[R]^{-1} = [I_{2d}] + \begin{bmatrix} [D] & -[H] \\ -[H'] & [D'] \end{bmatrix} \quad (34)$$

270 *Proof.* It is straightforward by using the decomposition (15) of \mathbf{A}_n and by
 271 substituting the solution of $\{\alpha_k\}$ in the asymmetric form of numerical flux (23b).
 272 \square

273 For several specific case, the following corollaries are immediate from Theo-
 274 rem 3.2:

275 **Corollary 3.2.1.** *On an element interface with continuous material properties,*
 276 *we have $[B] = [B'] = 0$, ${}^* \mathbf{L}_{n,k}^- = {}^{**} \mathbf{L}_{n,k}^- = \mathbf{L}_{n,k}^-$ and ${}^* \mathbf{L}_{n',k}^- = {}^{**} \mathbf{L}_{n',k}^- = \mathbf{L}_{n',k}^-$, so*
 277 *the characteristic coefficients $\{\alpha_k, \alpha'_k\}_{k=qL, qT_1, qT_2}$ of the Riemann problem (21)*
 278 *can be explicitly solved:*

$$\alpha_k = \mathbf{L}_{n,k}^- \cdot (\mathbf{U}_h - \mathbf{U}'_h), \quad \alpha'_k = \mathbf{L}_{n',k}^- \cdot (\mathbf{U}'_h - \mathbf{U}_h) \quad (35)$$

All the three fluxes defined in Theorem 3.2 are identical. They are all equal to
 the Käser's flux (30) and can be written as follows:

$$\hat{\mathbf{F}}_n(\mathbf{U}_h, \mathbf{U}'_h) = \hat{\mathbf{F}}_n^{\text{Käser}}(\mathbf{U}_h, \mathbf{U}'_h) \quad (36a)$$

$$= \lambda_{n,k}^+ (\mathbf{R}_{n,k}^+ \otimes \mathbf{L}_{n,k}^+) \cdot \mathbf{U}_h - \lambda_{n',k}^+ (\mathbf{R}_{n',k}^+ \otimes \mathbf{L}_{n',k}^+) \cdot \mathbf{U}'_h \quad (36b)$$

279 *Proof.* (36a) is straightforward. The symmetric form of the numerical flux (36b)
 280 can be obtained by remarking that, in the case of continuous material properties,
 281 the following equations hold (see Appendix A2):

$$\lambda'_{n',k} = \lambda_{n,k}, \quad \mathbf{R}_{n',k}^{\mp} = -\mathbf{R}_{n,k}^{\pm}, \quad \mathbf{L}_{n',k}^{\mp} = -\mathbf{L}_{n,k}^{\pm} \quad (37)$$

282

\square

283 **Corollary 3.2.2.** *On an element interface with discontinuous but isotropic ma-*
 284 *terial properties on its two sides, we have $[B] = [B'] = 0$, so the characteristic*
 285 *coefficients $\{\alpha_k, \alpha'_k\}_{k=qL, qT_1, qT_2}$ of the Riemann problem (21) can be explicitly*
 286 *solved:*

$$\alpha_k = {}^* \mathbf{L}_{n,k}^- \cdot \mathbf{U}_h - {}^{**} \mathbf{L}_{n,k}^- \cdot \mathbf{U}'_h, \quad \alpha'_k = {}^* \mathbf{L}_{n',k}^- \cdot \mathbf{U}'_h - {}^{**} \mathbf{L}_{n',k}^- \cdot \mathbf{U}_h \quad (38)$$

287 All the three fluxes defined in Theorem 3.2 are identical, and the 1st-order flux
 288 $\hat{\mathbf{F}}_n^{\text{1st-order}}(\mathbf{U}_h, \mathbf{U}'_h)$ defined by (31) is the exact solution of the Riemann problem
 289 (21).

290 *Proof.* It is straightforward by simply recalling that in the isotropic case $\gamma_{n,qL} =$
 291 \mathbf{n} , $\gamma_{n,qT_1} = \mathbf{t}_1$ and $\gamma_{n,qT_2} = \mathbf{t}_2$ \square

292

293 In the case of media with discontinuous anisotropic material properties, the
 294 sub-matrices $[B]$ and $[B']$ of $[\Delta R]$ defined by (27) are proportional to the degree
 295 of discontinuity across a physical interface. Thus, when the degree of discontinuity
 296 is sufficiently low, the 2nd-order flux, even the 1st-order flux, would be
 297 a sufficiently good numerical flux. However, when the degree of discontinuity
 298 is high, it is necessary to use the numerical flux that is the exact solution of
 299 the Riemann problem. It is worth noticing that the Käser's numerical flux (30)
 300 should be worse than the 1st-order flux (31), as it does not use the perturbed
 301 left eigenmodes $\{*\mathbf{L}_{n,k}^-, **\mathbf{L}_{n,k}^-\}$.

302 Finally, the most important remark concerning the numerical fluxes defined
 303 in Theorem 3.2 is that they are not physically sound in the case of media with
 304 discontinuous material properties. Indeed, on a physical interface, *i.e.* $\rho \neq \rho'$
 305 or/and $\mathbf{\Gamma}_n \neq \mathbf{\Gamma}'_n$, the interface conditions (25) derived from the equation (19c)
 306 of the Rankine–Hugoniot jump conditions (19) are not equivalent to the classical
 307 interface conditions of continuous velocity and stress vector. We recall that it
 308 has been shown in the 1D case [8] that the so-defined numerical flux was not
 309 able to give rise to physically sound wave propagation solutions.

310 Furthermore, the following result can be proved for the numerical flux (33)
 311 that is the exact solution of the Riemann problem:

312 **Theorem 3.3.** *The numerical flux (33) directly derived from the first-order*
 313 *velocity-stress system (1) is not consistent.*

314 *Proof.* To prove that a numerical flux $\hat{\mathbf{F}}_n(\mathbf{U}_h, \mathbf{U}'_h)$ is consistent, it should to
 315 be shown that:

$$\hat{\mathbf{F}}_n(\mathbf{U}, \mathbf{U}) = \mathbf{F}_n(\mathbf{U}) \quad (39)$$

316 According to (23b), it is necessary to have, when $\mathbf{U}_h = \mathbf{U}'_h = \mathbf{U}$ and for
 317 $k = qT, qT_1, qT_2$, $\alpha_{n,k} = 0$. But, this does not hold in the general case, as
 318 the second member of the system of linear equations (26), becoming in this
 319 case $\{(*\mathbf{L}_{n,k}^- - **\mathbf{L}_{n,k}^-) \cdot \mathbf{U}\}, \{(*\mathbf{L}'_{n',k} - **\mathbf{L}'_{n',k}) \cdot \mathbf{U}\}$, generally does not equal
 320 to zero. In other words, if $\alpha_{n,k} = 0$ and $\alpha'_{n',k} = 0$ for $k = qT, qT_1, qT_2$ with
 321 $\mathbf{U}_h = \mathbf{U}'_h = \mathbf{U}$, (21) then results in the following equation:

$$\mathbf{A}_n(\mathbf{U}|_E) + \mathbf{A}'_{n'}(\mathbf{U}|_{E'}) = \mathbf{0} \quad (40)$$

322 that is equivalent to:

$$\frac{\boldsymbol{\sigma}|_E \cdot \mathbf{n}}{\rho} + \frac{\boldsymbol{\sigma}|_{E'} \cdot \mathbf{n}'}{\rho'} = \mathbf{0}, \quad \rho \mathbf{\Gamma}_n \cdot \mathbf{v}|_E - \rho' \mathbf{\Gamma}'_{n'} \cdot \mathbf{v}|_{E'} = \mathbf{0} \quad (41)$$

323 But (41) is generally not true when the element interface is also a physical
 324 interface. \square

325 3.2. Upwind flux based on the mechanical interface conditions

326 In order to remove the physical inconsistency of the interface conditions (25),
 327 they are modified in the following way to take into account the classical interface
 328 conditions, *i.e.* velocity and stress vector continuities:

$$\boldsymbol{\sigma}_h^c \cdot \mathbf{n} + \boldsymbol{\sigma}_h^{c'} \cdot \mathbf{n}' = \mathbf{0}, \quad \mathbf{v}_h^c - \mathbf{v}_h^{c'} = \mathbf{0} \quad (42)$$

329 Both interface conditions (25) and (42) are equivalent only in the case where
 330 the elastic moduli and the density of the propagating medium are continuous
 331 across the interface.

It is easy to show that the interface conditions (42) is in fact a consequence
 of the following Rankine–Hugoniot jump conditions:

$$\tilde{\mathbf{A}}_{\mathbf{n}}(\mathbf{U}_h) - \tilde{\mathbf{A}}_{\mathbf{n}}(\mathbf{U}_h^c) = \tilde{\alpha}_k \lambda_{\mathbf{n},k}^- \tilde{\mathbf{M}}(\mathbf{R}_{\mathbf{n},k}^-) \quad (43a)$$

$$\tilde{\mathbf{A}}_{\mathbf{n}}(\mathbf{U}_h^c) + \tilde{\mathbf{A}}'_{\mathbf{n}'}(\mathbf{U}_h^c) = \mathbf{0} \quad (43b)$$

$$\tilde{\mathbf{A}}'_{\mathbf{n}'}(\mathbf{U}'_h) - \tilde{\mathbf{A}}'_{\mathbf{n}'}(\mathbf{U}_h^c) = \tilde{\alpha}'_k \lambda_{\mathbf{n}',k}^- \tilde{\mathbf{M}}'(\mathbf{R}_{\mathbf{n}',k}^-) \quad (43c)$$

332 which correspond to another equivalent form of the first-order velocity-stress
 333 system (1):

$$\tilde{\mathbf{M}}(\partial_t \mathbf{U}) + \tilde{\mathbf{A}}^{\partial_x}(\mathbf{U}) = \mathbf{0} \quad \text{or} \quad \begin{cases} \rho \partial_t \mathbf{v} - \text{Div}_x \boldsymbol{\sigma} = \mathbf{0} \\ \mathbf{C}^{-1} : \partial_t \boldsymbol{\sigma} - \boldsymbol{\varepsilon}(\mathbf{v}) = \mathbf{0} \end{cases} \quad (44)$$

334 with the following definitions of operators:

$$\tilde{\mathbf{M}} \begin{pmatrix} \mathbf{w} \\ \boldsymbol{\tau} \end{pmatrix} = \begin{pmatrix} \rho \mathbf{w} \\ \mathbf{C}^{-1} : \boldsymbol{\tau} \end{pmatrix}, \quad \tilde{\mathbf{A}}^{\partial_x} \begin{pmatrix} \mathbf{w} \\ \boldsymbol{\tau} \end{pmatrix} = \begin{pmatrix} -\text{Div}_x \boldsymbol{\tau} \\ -\boldsymbol{\varepsilon}(\mathbf{w}) \end{pmatrix}, \quad \tilde{\mathbf{A}}_{\mathbf{n}} \begin{pmatrix} \mathbf{w} \\ \boldsymbol{\tau} \end{pmatrix} = \begin{pmatrix} -\boldsymbol{\tau} \cdot \mathbf{n} \\ -\mathbf{n} \otimes_s \mathbf{w} \end{pmatrix} \quad (45)$$

335 We note that the following equations hold:

$$\tilde{\mathbf{M}}(\mathbf{R}_{\mathbf{n},k}) = \rho \mathbf{L}_{\mathbf{n},k}, \quad \tilde{\mathbf{A}}_{\mathbf{n}} = \tilde{\mathbf{M}} \cdot \mathbf{A}_{\mathbf{n}} = z_{\mathbf{n},k}^{\pm} \mathbf{L}_{\mathbf{n},k}^{\pm} \otimes \mathbf{L}_{\mathbf{n},k}^{\pm} \quad (46)$$

336 When the characteristic coefficients $\{\tilde{\alpha}_k, \tilde{\alpha}'_k\}_{k=qL, qT_1, qT_2}$ are calculated, the
 337 upwind numerical fluxes to be used for the first-order velocity-stress strong form
 338 (44) can be defined in the same way as in the preceding section, by taking into
 339 account (43a):

$$\hat{\tilde{\mathbf{F}}}_{\mathbf{n}}(\mathbf{U}_h, \mathbf{U}'_h) = \tilde{\mathbf{A}}_{\mathbf{n}}(\mathbf{U}_h^c) = \tilde{\mathbf{A}}_{\mathbf{n}}(\mathbf{U}_h) - \tilde{\alpha}_k z_{\mathbf{n},k}^- \mathbf{L}_{\mathbf{n},k}^- \quad (47)$$

340 However, it is also possible to keep using the variational formulation (9)
 341 of the first-order velocity-stress strong form (1) instead of the corresponding
 342 variational formulation of (44). In this case, by taking into account (46), the
 343 equation to define upwind numerical fluxes reads as:

$$\hat{\tilde{\mathbf{F}}}_{\mathbf{n}}(\mathbf{U}_h, \mathbf{U}'_h) = \tilde{\mathbf{M}}^{-1} \cdot \hat{\tilde{\mathbf{F}}}_{\mathbf{n}}(\mathbf{U}_h, \mathbf{U}'_h) = \mathbf{A}_{\mathbf{n}}(\mathbf{U}_h) - \tilde{\alpha}_k \lambda_{\mathbf{n},k}^- \mathbf{R}_{\mathbf{n},k}^- \quad (48)$$

344 It should be noted that both choices, the strong form (1) with the numerical
 345 flux (47) or the strong form (44) with the numerical flux (48), are equivalent,
 346 and their numerical implementations give rise to identical results, which is con-
 347 firmed by our numerical investigation. Moreover, we notice that $\hat{\tilde{\mathbf{F}}}_{\mathbf{n}'}(\mathbf{U}'_h, \mathbf{U}_h) \neq$
 348 $-\hat{\tilde{\mathbf{F}}}_{\mathbf{n}}(\mathbf{U}_h, \mathbf{U}'_h)$, even if the numerical flux (47) is conservative, *i.e.*, $\hat{\tilde{\mathbf{F}}}_{\mathbf{n}'}(\mathbf{U}'_h, \mathbf{U}_h) =$
 349 $-\hat{\tilde{\mathbf{F}}}_{\mathbf{n}}(\mathbf{U}_h, \mathbf{U}'_h)$.

350 To solve the Riemann problem (43), the same technique presented in the
 351 preceding section is used, and the following result concerning the mechanically
 352 based Riemann problem can be proved:

353 **Theorem 3.4.** *The characteristic coefficients $\{\tilde{\alpha}_k, \tilde{\alpha}'_k\}_{k=qL, qT_1, qT_2}$ of the Rie-*
 354 *mann problem (43) are the solution of the following linear system of equations:*

$$\begin{bmatrix} [I_d] & [\tilde{B}] \\ [\tilde{B}'] & [I_d] \end{bmatrix} \cdot \begin{pmatrix} \{\tilde{\alpha}_k\} \\ \{\tilde{\alpha}'_k\} \end{pmatrix} = \begin{pmatrix} \{\tilde{\mathbf{L}}_{\mathbf{n},k}^- \cdot (\mathbf{U}_h - \mathbf{U}'_h)\} \\ \{\tilde{\mathbf{L}}_{\mathbf{n}',k}^- \cdot (\mathbf{U}'_h - \mathbf{U}_h)\} \end{pmatrix} \quad (49)$$

356 In (49), $[I_d]$ is the $d \times d$ identity matrix and $[\tilde{B}]$ and $[\tilde{B}']$ are $d \times d$ matrices
 357 with zero diagonal terms and the following extra-diagonal terms:

$$\tilde{B}_{kl, k \neq l} = -\frac{C_{z,k}^-}{2} \frac{\delta z_{\mathbf{n}',kl}^-}{z_{\mathbf{n}',k}^-} \gamma_{\mathbf{n},k} \cdot \gamma_{\mathbf{n}',l}, \quad \tilde{B}'_{kl, k \neq l} = -\frac{C_{z,k}^{-'}}{2} \frac{\delta z_{\mathbf{n},kl}^-}{z_{\mathbf{n},k}^-} \gamma_{\mathbf{n}',k} \cdot \gamma_{\mathbf{n},l} \quad (50)$$

358 where $C_{z,k}^-$, $C_{z,k}^{-'}$, $\delta z_{\mathbf{n}',kl}^-$ and $\delta z_{\mathbf{n},kl}^-$ are defined in Theorem 3.1. $\{\tilde{\mathbf{L}}_{\mathbf{n},k}^-, \tilde{\mathbf{L}}_{\mathbf{n}',k}^-\}$
 359 are the perturbed left eigenmodes of $\{\mathbf{A}_{\mathbf{n}}, \mathbf{A}'_{\mathbf{n}}\}$ calculated by using the material
 360 properties of the adjacent element in the following way:

$$\tilde{\mathbf{L}}_{\mathbf{n},k}^- = \begin{pmatrix} C_{z,k}^- \mathfrak{P}_{vect}(\mathbf{L}_{\mathbf{n},k}^-) \\ C_{z,k}^{-'} \mathfrak{P}_{tens}(\mathbf{L}_{\mathbf{n},k}^-) \end{pmatrix}, \quad \tilde{\mathbf{L}}_{\mathbf{n}',k}^- = \begin{pmatrix} C_{z,k}^{-'} \mathfrak{P}_{vect}(\mathbf{L}_{\mathbf{n}',k}^-) \\ C_{z,k}^- \mathfrak{P}_{tens}(\mathbf{L}_{\mathbf{n}',k}^-) \end{pmatrix} \quad (51)$$

361 *Proof.* See Appendix A3. □

362
 363 As in the preceding section, by decomposing the $2d \times 2d$ matrix of the system
 364 of linear equations (49) as $[\tilde{R}] = [I_{2d}] + [\Delta \tilde{R}]$, the following upwind numerical
 365 fluxes are proposed:

Theorem 3.5. *According to how the inverse of $[\tilde{R}]$ the matrix of the system of*
 (49) *is approached, three upwind numerical fluxes can be defined as follows:*

1) *1st-order upwind numerical flux by taking $[\tilde{R}]^{-1} \approx [I_{2d}]$ and by remarking*
 that $[\tilde{R}] \cdot [I_{2d}] - [I_{2d}] = [\Delta \tilde{R}]$

$$\hat{\hat{\mathbf{F}}}_{\mathbf{n}}(\mathbf{U}_h, \mathbf{U}'_h) = \tilde{\mathbf{M}}(\hat{\mathbf{F}}_{\mathbf{n}}^{K\u00e4ser}(\mathbf{U}_h, \mathbf{U}'_h)) + z_{\mathbf{n},k}^- (\mathbf{L}_{\mathbf{n},k}^- \otimes (\mathbf{L}_{\mathbf{n},k}^- - \tilde{\mathbf{L}}_{\mathbf{n},k}^-)) \cdot (\mathbf{U}_h - \mathbf{U}'_h) \quad (52a)$$

$$\hat{\mathbf{F}}_{\mathbf{n}}(\mathbf{U}_h, \mathbf{U}'_h) = \hat{\mathbf{F}}_{\mathbf{n}}^{K\u00e4ser}(\mathbf{U}_h, \mathbf{U}'_h) + \lambda_{\mathbf{n},k}^- (\mathbf{R}_{\mathbf{n},k}^- \otimes (\mathbf{L}_{\mathbf{n},k}^- - \tilde{\mathbf{L}}_{\mathbf{n},k}^-)) \cdot (\mathbf{U}_h - \mathbf{U}'_h) \quad (52b)$$

2) *2nd-order upwind numerical flux by taking $[\tilde{R}]^{-1} \approx [I_{2d}] - [\Delta \tilde{R}]$ and by*
 remarking that $[\tilde{R}] \cdot ([I_{2d}] - [\Delta \tilde{R}]) - [I_{2d}] = [\Delta \tilde{R}]^2$

$$\hat{\hat{\mathbf{F}}}_{\mathbf{n}}(\mathbf{U}_h, \mathbf{U}'_h) = \hat{\hat{\mathbf{F}}}_{\mathbf{n}}^{1st-order}(\mathbf{U}_h, \mathbf{U}'_h) - z_{\mathbf{n},k}^- \sum_{l \neq k} \tilde{B}_{kl} (\mathbf{L}_{\mathbf{n},k}^- \otimes \tilde{\mathbf{L}}_{\mathbf{n}',l}^-) \cdot (\mathbf{U}_h - \mathbf{U}'_h) \quad (53a)$$

$$\hat{\mathbf{F}}_{\mathbf{n}}(\mathbf{U}_h, \mathbf{U}'_h) = \hat{\mathbf{F}}_{\mathbf{n}}^{1st-order}(\mathbf{U}_h, \mathbf{U}'_h) - \lambda_{\mathbf{n},k}^- \sum_{l \neq k} \tilde{B}_{kl} (\mathbf{R}_{\mathbf{n},k}^- \otimes \tilde{\mathbf{L}}_{\mathbf{n}',l}^-) \cdot (\mathbf{U}_h - \mathbf{U}'_h) \quad (53b)$$

where $\hat{\mathbf{F}}_{\mathbf{n}}^{1st-order}(\mathbf{U}_h, \mathbf{U}'_h)$ and $\hat{\mathbf{F}}_{\mathbf{n}}^{1st-order}(\mathbf{U}_h, \mathbf{U}'_h)$ denote the fluxes defined respectively by (52a) and (52b).

3) Upwind numerical flux being the exact solution of the Riemann problem(43)

$$\hat{\mathbf{F}}_{\mathbf{n}}(\mathbf{U}_h, \mathbf{U}'_h) = \hat{\mathbf{F}}_{\mathbf{n}}^{1st-order}(\mathbf{U}_h, \mathbf{U}'_h) - z_{\mathbf{n},k}^- \mathbf{L}_{\mathbf{n},k}^- \otimes (\tilde{D}_{kl} \tilde{\mathbf{L}}_{\mathbf{n},l}^- + \tilde{H}_{kl} \tilde{\mathbf{L}}_{\mathbf{n}',l}^-) \cdot (\mathbf{U}_h - \mathbf{U}'_h) \quad (54a)$$

$$\hat{\mathbf{F}}_{\mathbf{n}}(\mathbf{U}_h, \mathbf{U}'_h) = \hat{\mathbf{F}}_{\mathbf{n}}^{1st-order}(\mathbf{U}_h, \mathbf{U}'_h) - \lambda_{\mathbf{n},k}^- \mathbf{R}_{\mathbf{n},k}^- \otimes (\tilde{D}_{kl} \tilde{\mathbf{L}}_{\mathbf{n},l}^- + \tilde{H}_{kl} \tilde{\mathbf{L}}_{\mathbf{n}',l}^-) \cdot (\mathbf{U}_h - \mathbf{U}'_h) \quad (54b)$$

366 with $[\tilde{D}]$, $[\tilde{D}']$, $[\tilde{H}]$ and $[\tilde{H}']$ four $d \times d$ matrices defined by the following decom-
367 position of the inverse matrix of $[\tilde{R}]$:

$$[\tilde{R}]^{-1} = [I_{2d}] + \begin{bmatrix} [\tilde{D}] & -[\tilde{H}] \\ -[\tilde{H}'] & [\tilde{D}'] \end{bmatrix} \quad (55)$$

368 *Proof.* It is straightforward by using the decomposition (15) of $\mathbf{A}_{\mathbf{n}}$ and the
369 equations given by (46), and by substituting the solution of $\{\tilde{\alpha}_k\}$ in the equa-
370 tions of numerical fluxes (47) and (48). \square

371

372 As in the preceding section, the following corollaries can be proved for several
373 specific cases:

374 **Corollary 3.5.1.** *On an element interface with continuous material properties,*
375 *we have $[\tilde{B}] = [\tilde{B}'] = 0$, $\tilde{\mathbf{L}}_{\mathbf{n},k}^- = \mathbf{L}_{\mathbf{n},k}^-$ and $\tilde{\mathbf{L}}_{\mathbf{n}',k}^- = \mathbf{L}_{\mathbf{n}',k}^-$, so the characteristic*
376 *coefficients $\{\tilde{\alpha}_k, \tilde{\alpha}'_k\}_{k=qL, qT_1, qT_2}$ of the Riemann problem (43) can be explicitly*
377 *solved:*

$$\tilde{\alpha}_k = \mathbf{L}_{\mathbf{n},k}^- \cdot (\mathbf{U}_h - \mathbf{U}'_h), \quad \tilde{\alpha}'_k = \mathbf{L}_{\mathbf{n}',k}^- \cdot (\mathbf{U}'_h - \mathbf{U}_h) \quad (56)$$

378 *All the three fluxes defined in Theorem 3.5 are identical. They are equivalent to*
379 *the one defined by (36) in Corollary 3.2.1.*

380 **Corollary 3.5.2.** *On an element interface with discontinuous but isotropic ma-*
381 *terial properties on its two sides, we have $[\tilde{B}] = [\tilde{B}'] = 0$, so the characteristic*
382 *coefficients $\{\tilde{\alpha}_k, \tilde{\alpha}'_k\}_{k=qL, qT_1, qT_2}$ of the Riemann problem (43) can be explicitly*
383 *solved:*

$$\tilde{\alpha}_k = \tilde{\mathbf{L}}_{\mathbf{n},k}^- \cdot (\mathbf{U}_h - \mathbf{U}'_h), \quad \tilde{\alpha}'_k = \tilde{\mathbf{L}}_{\mathbf{n}',k}^- \cdot (\mathbf{U}'_h - \mathbf{U}_h) \quad (57)$$

384 *All the three fluxes defined in Theorem 3.5 are identical, and the 1st-order flux*
385 *$\hat{\mathbf{F}}_{\mathbf{n}}^{1st-order}(\mathbf{U}_h, \mathbf{U}'_h)$ defined by (52a) is the exact solution of the Riemann prob-*
386 *lem (43).*

387 Concerning the consistency of the numerical flux (54) that is the exact so-
388 lution of the Riemann problem, the following result can be proved.

389 **Theorem 3.6.** *The numerical flux (54) based on the mechanical interface con-*
390 *ditions and corresponding to the first-order velocity-stress system (44) is con-*
391 *sistent.*

392 *Proof.* As the second member of the system of linear equations (49) is equal to
 393 zero with $\mathbf{U}_h = \mathbf{U}'_h = \mathbf{U}$, hence, we have $\tilde{\alpha}_{\mathbf{n},k} = \tilde{\alpha}'_{\mathbf{n},k} = 0$ for $k = qT, qT_1, qT_2$.
 394 Then, according to (47) and (48), we get $\hat{\tilde{\mathbf{F}}}_{\mathbf{n}}(\mathbf{U}, \mathbf{U}) = \tilde{\mathbf{F}}_{\mathbf{n}}(\mathbf{U})$ and $\hat{\mathbf{F}}_{\mathbf{n}}(\mathbf{U}, \mathbf{U}) =$
 395 $\mathbf{F}_{\mathbf{n}}(\mathbf{U})$. \square

396 4. Upwind numerical fluxes for the first-order velocity-strain system

397 In this section, we apply the approach developed in the preceding section
 398 to the first-order velocity-strain wave equations defined in Section 2.2. In [6],
 399 an upwind numerical flux that is exact solution of the Riemann problem was
 400 developed in the case of isotropic heterogeneous media with discontinuous elastic
 401 moduli and density. Hereafter, the more general case of anisotropic media is
 402 considered. Firstly, the elastic wave oriented eigenanalysis is applied to the first-
 403 order velocity-strain waves equations (11). Secondly, the Riemann problem is
 404 defined and solved to develop upwind numerical fluxes.

405 4.1. Elastic wave oriented eigenanalysis of the first-order \mathbf{v} - $\boldsymbol{\varepsilon}$ system (11)

406 As in the case of the first-order velocity-stress system, before giving the
 407 definition of the Riemann problem at an element interface, eigenanalysis of
 408 the first-order velocity-strain system (11) is performed, *i.e.*, the solving of the
 409 following eigenproblem:

$$\mathbf{A}_{\mathbf{n}}(\mathbf{R}_{\mathbf{n},k}) = \lambda_{\mathbf{n},k} \mathbf{M}(\mathbf{R}_{\mathbf{n},k}), \quad \mathbf{A}_{\mathbf{n}}^T(\mathbf{L}_{\mathbf{n},k}) = \lambda_{\mathbf{n},k} \mathbf{M}(\mathbf{L}_{\mathbf{n},k}) \quad (58)$$

410 with $\mathbf{A}_{\mathbf{n}}$ and \mathbf{M} defined respectively in (13) and (12). The following results
 411 can be proved.

412 Among the $m = d + d(d+1)/2$ eigenvalues of the eigensystem (58), there are
 413 d strictly negative eigenvalues $(\lambda_{\mathbf{n},k}^- = -c_{\mathbf{n},k})_{k=qL, \{qT_{\alpha}\}_{\alpha=1, \dots, d-1}}$ and d strictly
 414 positive eigenvalues $(\lambda_{\mathbf{n},k}^+ = c_{\mathbf{n},k})_{k=qL, \{qT_{\alpha}\}_{\alpha=1, \dots, d-1}}$, $c_{\mathbf{n},qL}$ and $c_{\mathbf{n},qT_{\alpha}}$ being
 415 respectively the velocity of quasi longitudinal and quasi transverse wave modes
 416 propagating in the \mathbf{n} direction. The right and left eigenmodes corresponding to
 417 these nonzero eigenvalues are: $\forall k = qL, \{qT_{\alpha}\}_{\alpha=1, \dots, d-1}$

$$\mathbf{R}_{\mathbf{n},k}^{\pm} = \begin{pmatrix} \mathbf{w}_{\mathbf{n},k} \\ -\rho(z_{\mathbf{n},k}^{\pm})^{-1} \mathbf{n} \otimes_s \mathbf{w}_{\mathbf{n},k} \end{pmatrix}, \quad \mathbf{L}_{\mathbf{n},k}^{\pm} = \rho^{-1} \begin{pmatrix} \mathbf{w}_{\mathbf{n},k} \\ -\rho(z_{\mathbf{n},k}^{\pm})^{-1} \mathbf{C} : (\mathbf{n} \otimes_s \mathbf{w}_{\mathbf{n},k}) \end{pmatrix} \quad (59)$$

418 As in the previous case of the first-order velocity-stress system, $\mathbf{w}_{\mathbf{n},k} = \frac{1}{\sqrt{2}} \boldsymbol{\gamma}_{\mathbf{n},k}$,
 419 with $(\boldsymbol{\gamma}_{\mathbf{n},k})_{k=qL, \{qT_{\alpha}\}_{\alpha=1, \dots, d-1}}$ the unit eigenvectors of the Christoffel tensor $\boldsymbol{\Gamma}_{\mathbf{n}}$.
 420 It can be shown that the following orthonormality relation holds between the
 421 two right and left eigenbases:

$$\mathbf{R}_{\mathbf{n},k} \cdot \mathbf{M}(\mathbf{L}_{\mathbf{n},l}) = \delta_{kl}, \forall k, l = 1, \dots, m \quad (60)$$

422 where δ_{kl} denotes the usual Kronecker delta. Hence, using its two eigenbases, the
 423 normal Jacobian operator $\mathbf{A}_{\mathbf{n}}$ defined by (13) of the first-order velocity-strain
 424 wave equations (11) can be decomposed as follows:

$$\mathbf{A}_{\mathbf{n}} = \lambda_{\mathbf{n},k}^- \mathbf{M}(\mathbf{R}_{\mathbf{n},k}^-) \otimes \mathbf{M}(\mathbf{L}_{\mathbf{n},k}^-) + \lambda_{\mathbf{n},k}^+ \mathbf{M}(\mathbf{R}_{\mathbf{n},k}^+) \otimes \mathbf{M}(\mathbf{L}_{\mathbf{n},k}^+) \quad (61)$$

425 *4.2. Upwind numerical fluxes*

In the 3D case, the Riemann problem corresponding to the first-order velocity-strain equations (11), *i.e.*, the Rankine-Hugoniot jump conditions across an element interface (Figure 1), reads as:

$$\mathbf{A}_n(\mathbf{U}_h) - \mathbf{A}_n(\mathbf{U}_h^c) = \alpha_k \lambda_{n,k}^- \mathbf{M}(\mathbf{R}_{n,k}^-) \quad (62a)$$

$$\mathbf{A}_n(\mathbf{U}_h^c) + \mathbf{A}'_{n'}(\mathbf{U}_h^c) = \mathbf{0} \quad (62b)$$

$$\mathbf{A}'_{n'}(\mathbf{U}'_h) - \mathbf{A}'_{n'}(\mathbf{U}_h^c) = \alpha'_k \lambda_{n',k}^- \mathbf{M}'(\mathbf{R}_{n',k}^-) \quad (62c)$$

426 (62b) gives rise to the following interface conditions that are clearly physically
427 sound:

$$(\mathbf{C} : \boldsymbol{\varepsilon}_h^c) \cdot \mathbf{n} + (\mathbf{C}' : \boldsymbol{\varepsilon}'_h) \cdot \mathbf{n}' = \mathbf{0}, \quad \mathbf{v}_h^c - \mathbf{v}'_h = \mathbf{0} \quad (63)$$

428 When the characteristic coefficients $\{\alpha_k, \alpha'_k\}_{k=qL, qT_1, qT_2}$ are calculated, up-
429 wind numerical fluxes can be defined in the same way as in the preceding section,
430 by taking into account (62a):

$$\hat{\mathbf{F}}_n(\mathbf{U}_h, \mathbf{U}'_h) = \mathbf{A}_n(\mathbf{U}_h^c) = \mathbf{A}_n(\mathbf{U}_h) - \alpha_{n,k} \lambda_{n,k}^- \mathbf{M}(\mathbf{R}_{n,k}^-) \quad (64)$$

431 When the Riemann problem is exactly solved by the numerical flux, the latter
432 is conservative, as we have, due to (62b), $\hat{\mathbf{F}}_{n'}(\mathbf{U}'_h, \mathbf{U}_h) = -\hat{\mathbf{F}}_n(\mathbf{U}_h, \mathbf{U}'_h)$.

433 To solve the Riemann problem (62), the same technique presented in the
434 preceding section is used, and the following result can be proved:

435 **Theorem 4.1.** *The characteristic coefficients $\{\alpha_k, \alpha'_k\}_{k=qL, qT_1, qT_2}$ of the Rie-*
436 *mann problem (62) are the solution of the following linear system of equations:*

$$\begin{bmatrix} [I_d] & [\tilde{B}] \\ [\tilde{B}'] & [I_d] \end{bmatrix} \cdot \begin{pmatrix} \{\alpha_k\} \\ \{\alpha'_k\} \end{pmatrix} = \begin{pmatrix} \{\mathbf{M}(*\mathbf{L}_{n,k}^-) \cdot (\mathbf{U}_h - \mathbf{U}'_h)\} \\ \{\mathbf{M}'(*\mathbf{L}'_{n',k}^-) \cdot (\mathbf{U}'_h - \mathbf{U}_h)\} \end{pmatrix} \quad (65)$$

438 In (65), $[I_d]$ is the $d \times d$ identity matrix and $[\tilde{B}]$ and $[\tilde{B}']$ are the two $d \times d$
439 matrices already defined in Theorem 3.4. The operators \mathbf{M} and \mathbf{M}' are defined
440 in (12). $\{\mathbf{L}_{n,k}^-, * \mathbf{L}'_{n',k}^-\}$ are the perturbed left eigenmodes of the eigensystem
441 (58) calculated by using the material properties of the adjacent element in the
442 following way:

$$*\mathbf{L}_{n,k}^- = \begin{pmatrix} C_{z,k}^- \boldsymbol{\rho}_{vect}(\mathbf{L}_{n,k}^-) \\ C_{z,k}^- \boldsymbol{\rho}_{tens}(\mathbf{L}_{n,k}^-) \end{pmatrix}, \quad *\mathbf{L}'_{n',k}^- = \begin{pmatrix} C_{z,k}^- \boldsymbol{\rho}_{vect}(\mathbf{L}'_{n',k}^-) \\ C_{z,k}^- \boldsymbol{\rho}_{tens}(\mathbf{L}'_{n',k}^-) \end{pmatrix} \quad (66)$$

443 *Proof.* See Appendix A4. □

444 We remark that, on the one side, both systems of linear equations (49) of
445 Theorem 3.4 and (65) of Theorem 4.1 have the same $2d \times 2d$ matrix $[\tilde{R}]$, and on
446 the other hand, the equation (66) has the same form as the equation (51) but
447 applies to the left eigenmodes defined by (59).

448 As in the preceding section, by decomposing $[\tilde{R}]$ into $[I_{2d}] + [\Delta \tilde{R}]$, the fol-
449 lowing upwind numerical fluxes are proposed:
450

451 **Theorem 4.2.** According to how the inverse of $[\tilde{R}]$ the matrix of the system of
 452 (65) is approached, three upwind numerical fluxes can be defined as follows:
 453 1) 1st-order upwind numerical flux by taking $[\tilde{R}]^{-1} \approx [I_{2d}]$ and by remarking
 454 that $[\tilde{R}].[I_{2d}] - [I_{2d}] = [\Delta\tilde{R}]$

$$\begin{aligned} \hat{\mathbf{F}}_{\mathbf{n}}(\mathbf{U}_h, \mathbf{U}'_h) &= \lambda_{\mathbf{n},k}^+(M(\mathbf{R}_{\mathbf{n},k}^+) \otimes M(\mathbf{L}_{\mathbf{n},k}^+)) \cdot \mathbf{U}_h + \lambda_{\mathbf{n},k}^-(M(\mathbf{R}_{\mathbf{n},k}^-) \otimes M(\mathbf{L}_{\mathbf{n},k}^-)) \cdot \mathbf{U}'_h \\ &\quad + \lambda_{\mathbf{n},k}^-(M(\mathbf{R}_{\mathbf{n},k}^-) \otimes M(\mathbf{L}_{\mathbf{n},k}^- * \mathbf{L}_{\mathbf{n},k}^-)) \cdot (\mathbf{U}_h - \mathbf{U}'_h) \end{aligned} \quad (67)$$

455 2) 2nd-order upwind numerical flux by taking $[\tilde{R}]^{-1} \approx [I_{2d}] - [\Delta\tilde{R}]$ and by
 456 remarking that $[\tilde{R}].[I_{2d}] - [\Delta\tilde{R}].[I_{2d}] = [\Delta\tilde{R}]^2$

$$\hat{\mathbf{F}}_{\mathbf{n}}(\mathbf{U}_h, \mathbf{U}'_h) = \hat{\mathbf{F}}_{\mathbf{n}}^{1st-order}(\mathbf{U}_h, \mathbf{U}'_h) - \lambda_{\mathbf{n},k}^- \sum_{l \neq k} \tilde{B}_{kl} (M(\mathbf{R}_{\mathbf{n},k}^-) \otimes M(*\mathbf{L}_{\mathbf{n}',l}^-)) \cdot (\mathbf{U}_h - \mathbf{U}'_h) \quad (68)$$

457 where $\hat{\mathbf{F}}_{\mathbf{n}}^{1st-order}(\mathbf{U}_h, \mathbf{U}'_h)$ denotes the flux defined by (67).

458 3) Upwind numerical flux being the exact solution of the Riemann problem (62)

$$\begin{aligned} \hat{\mathbf{F}}_{\mathbf{n}}(\mathbf{U}_h, \mathbf{U}'_h) &= \hat{\mathbf{F}}_{\mathbf{n}}^{1st-order}(\mathbf{U}_h, \mathbf{U}'_h) \\ &\quad - \lambda_{\mathbf{n},k}^- M(\mathbf{R}_{\mathbf{n},k}^-) \otimes (\tilde{D}_{kl} M(*\mathbf{L}_{\mathbf{n},l}^-) + \tilde{H}_{kl} M(*\mathbf{L}_{\mathbf{n}',l}^-)) \cdot (\mathbf{U}_h - \mathbf{U}'_h) \end{aligned} \quad (69)$$

459 with $[\tilde{D}]$, $[\tilde{D}']$, $[\tilde{H}]$ and $[\tilde{H}']$ four $d \times d$ matrices already defined in Theorem 3.4.

460 *Proof.* It is straightforward by using the decomposition (61) of $\mathbf{A}_{\mathbf{n}}$ and by sub-
 461 stituting the solution of $\{\alpha_k\}$ in the equation of numerical flux (64). \square

462

463 As in the preceding section, the following corollaries can be proved for several
 464 specific cases:

465 **Corollary 4.2.1.** On an element interface with continuous material properties,
 466 we have $[\tilde{B}] = [\tilde{B}'] = 0$, $*\mathbf{L}_{\mathbf{n},k}^- = \mathbf{L}_{\mathbf{n},k}^-$ and $*\mathbf{L}_{\mathbf{n}',k}^- = \mathbf{L}_{\mathbf{n}',k}^-$, so the characteristic
 467 coefficients $\{\alpha_k, \alpha'_k\}_{k=qL, qT_1, qT_2}$ of the Riemann problem (62) can be explicitly
 468 solved:

$$\alpha_k = M(\mathbf{L}_{\mathbf{n},k}^-) \cdot (\mathbf{U}_h - \mathbf{U}'_h), \quad \alpha'_k = M'(\mathbf{L}_{\mathbf{n}',k}^-) \cdot (\mathbf{U}'_h - \mathbf{U}_h) \quad (70)$$

All the three fluxes defined in Theorem 4.2 are identical and can be written as
 follows:

$$\hat{\mathbf{F}}_{\mathbf{n}}(\mathbf{U}_h, \mathbf{U}'_h) = \lambda_{\mathbf{n},k}^+(M(\mathbf{R}_{\mathbf{n},k}^+) \otimes M(\mathbf{L}_{\mathbf{n},k}^+)) \cdot \mathbf{U}_h + \lambda_{\mathbf{n},k}^-(M(\mathbf{R}_{\mathbf{n},k}^-) \otimes M(\mathbf{L}_{\mathbf{n},k}^-)) \cdot \mathbf{U}'_h \quad (71a)$$

$$= \lambda_{\mathbf{n},k}^+(M(\mathbf{R}_{\mathbf{n},k}^+) \otimes M(\mathbf{L}_{\mathbf{n},k}^+)) \cdot \mathbf{U}_h - \lambda_{\mathbf{n}',k}^+(M'(\mathbf{R}_{\mathbf{n}',k}^+) \otimes M'(\mathbf{L}_{\mathbf{n}',k}^+)) \cdot \mathbf{U}'_h \quad (71b)$$

469 **Corollary 4.2.2.** On an element interface with discontinuous but isotropic ma-
 470 terial properties on its two sides, we have $[\tilde{B}] = [\tilde{B}'] = 0$, so the characteristic

471 coefficients $\{\tilde{\alpha}_k, \tilde{\alpha}'_k\}_{k=qL, qT_1, qT_2}$ of the Riemann problem (62) can be explicitly
 472 solved:

$$\alpha_k = \mathbf{M}(\mathbf{L}_{\mathbf{n},k}^-) \cdot (\mathbf{U}_h - \mathbf{U}'_h), \quad \alpha'_k = \mathbf{M}'(\mathbf{L}'_{\mathbf{n}',k}) \cdot (\mathbf{U}'_h - \mathbf{U}_h) \quad (72)$$

473 All the three fluxes defined in Theorem 4.2 are identical, and the 1st-order flux
 474 $\hat{\mathbf{F}}_{\mathbf{n}}^{1st-order}(\mathbf{U}_h, \mathbf{U}'_h)$ defined by (67) is the exact solution of the Riemann problem
 475 (62).

476 We remark that the case of Corollary 4.2.2 was treated by Wilcox *et al.*
 477 in [6]. Our equation of numerical flux (67) is more compact and highlights the
 478 important role played by the gap between the acoustic impedances on both sides
 479 of element interfaces.

480 Concerning the consistency of the numerical flux (54) that is the exact so-
 481 lution of the Riemann problem, the following result can be proved.

482 **Theorem 4.3.** *The numerical flux (69) of the first-order velocity-strain system*
 483 *(11) is consistent.*

484 *Proof.* The second member of the system of linear equations (65) is equal to
 485 zero, so $\alpha_{\mathbf{n},k} = \alpha'_{\mathbf{n},k} = 0$ for $k = qT, qT_1, qT_2$. Then, according to (64), we get
 486 $\hat{\mathbf{F}}_{\mathbf{n}}(\mathbf{U}, \mathbf{U}) = \mathbf{F}_{\mathbf{n}}(\mathbf{U})$. □

487 5. Numerical investigations of the numerical fluxes

488 The objectif of this section is to numerically validate the numerical fluxes
 489 proposed in the present work, especially the one solving exactly the Riemann
 490 problem and giving rise to the appropriate mechanical interface conditions ((54)
 491 in Section 3.2), which is named “MG_sDG” hereafter.

492 In the present work, the time domain solving of the variational dG formu-
 493 lation (9b) is done by using the standard four-stage fourth-order Runge-Kutta
 494 iterative method, which is only conditionally stable. According to [16], the
 495 following stability condition written in the general context of anisotropic and
 496 piecewise homogeneous media should be satisfied:

$$\Delta t_{sDG} \leq \frac{CFL_{sDG}}{2N_p + 1} \min_E \left\{ \frac{h^E}{\max_{\mathbf{n}} \{c_{\mathbf{n},L}^E\}} \right\} \quad (73)$$

497 with N_p the order of the FE basis function, h^E the size of the element E and
 498 CFL_{sDG} the Courant-Friedrichs-Levy number. For the numerical examples
 499 presented hereafter, FE meshes with four-node quadrilateral (Q4) elements are
 500 systematically used. Hence, we have $N_p = 1$. The constant CFL_{sDG} depends
 501 on the order of FE basis function, the space dimension d ($d = 1, 2, 3$), as well as
 502 the shape of finite element. According to our numerical experiences, $CFL_{sDG} =$
 503 0.6 always works in the 2D case with $N_p = 1$, *i.e.*, for three-node triangular
 504 (T3) elements or Q4 elements.

505 The element size h^E should be chosen by considering the shortest wavelength
 506 of interest, which is, in turn, defined by the highest frequency of interest often
 507 determined by the frequency content of external loadings. For the numerical
 508 examples presented hereafter, ricker signals are used to define the dependency
 509 of the external loadings upon the time t , *i.e.*:

$$\mathbf{g}(\mathbf{x}, t) = \mathbf{a}_g(\mathbf{x}) \left(1 - 2 \left(\frac{2\pi(t - T_r/2)}{T_r} \right)^2 \right) e^{-\left(\frac{2\pi(t - T_r/2)}{T_r} \right)^2} \quad (74)$$

510 with T_r the period of the ricker signal. The advantage of using a ricker signal
 511 is to have a perfectly controlled frequency range with a central frequency equal
 512 to $f_{max} = 2T_r^{-1}$ and a cutoff frequency that can be reasonably taken equal to
 513 $f_c = 2.5f_{max}$. In the present work, the highest frequency of interest is chosen
 514 equal to f_c , and the associated shortest wavelength of quasi transverse waves is
 515 used to define the element size h^E .

516 Numerical results obtained with the use of the flux “MG_sDG” are compared
 517 to the reference numerical solutions calculated by using a time discontinuous
 518 space-time Galerkin solver (named “tDG” hereafter). The basic idea of this time
 519 discontinuous space-time Galerkin method is to subdivide the studied space-time
 520 domain $\Omega \times]0, T[$ into a series of space-time slabs $\Omega \times]t_n, t_{n+1}[$ and to write in
 521 each space-time slab a variational formulation by considering both displacement
 522 and velocity unknowns. Within each space-time slab, continuous finite elements
 523 are used, but between two successive slabs, both displacement and velocity fields
 524 are discontinuous [17, 18, 19, 20]. It can be shown that the time dG method
 525 is unconditionally stable, which constitutes a real advantage. Otherwise, due
 526 to energies dissipated in time jumps between two subsequent space-time slabs,
 527 there is also a numerical damping inherent to this method that increases with the
 528 frequency and allows filtering numerical spurious noises. The time dG solver
 529 used in this work discretizes the space with a finite element mesh combined
 530 with one linear element in time for each space-time slab. It can be formulated
 531 in the form of an implicit time-stepping schemes and has been validated by our
 532 previous studies [21, 22, 20] and also by other authors [19, 23].

533 As for the definition of the time step for the time dG solver, it is necessary to
 534 take a sufficiently small time step to prevent higher frequency modes of interest
 535 from its numerical damping. The following formula is systematically applied in
 536 our work:

$$\Delta t_{tDG} = \min_E \left\{ \frac{h^E}{\max_n \{c_{n,L}^E\}} \right\} \quad (75)$$

537 Therefore, for all the numerical examples presented hereafter, we have $\Delta t_{tDG} =$
 538 $5\Delta t_{sDG}$, when a same element size h^E is used.

539 5.1. Heterogeneous bimaterial case with anisotropic/isotropic materials

540 The first example was the one already calculated by Komatitsch *et al.*
 541 [24] and de la Puente *et al.* [5]. A square domain $\Omega =] - 0.325, 0.325[\times] -$
 542 $0.325, 0.325[\text{m}^2$ composed of two materials is considered. The two materials are

543 separated by the axis $x_1 = 0$: the one on the left is an anisotropic (transversely
544 isotropic) zinc crystal, and the one on the right is isotropic. Their material
545 properties are given in Table I. We remark that, for the transversely isotropic
546 material, the symmetry axis is in the x_2 -direction. For the anisotropic materi-
547 al, wave velocities and wave fronts are analytically calculated by considering
548 the anisotropic elastic tensor, and they are shown in Figure 2. Free boundary
549 conditions are applied on $\partial\Omega$.

	C_{1111} (GPa)	C_{1122} (GPa)	C_{2222} (GPa)	C_{1212} (GPa)	ρ (kg m ⁻³)
<i>isotropic</i>	165	85.8	165	39.6	7100
<i>anisotropic</i>	165	50	62	39.6	7100

Table I: Material properties of the isotropic and anisotropic materials of the bimaterial example

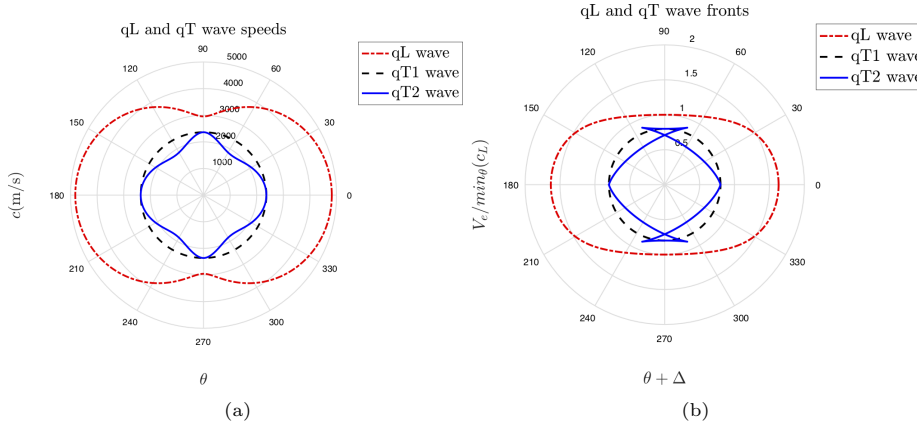


Figure 2: (a) Wave velocities, and (b) Waves fronts, of the anisotropic material (only curves in red blue are to be considered in the 2D problem defined in the Ox_1x_2 plan).

550 Not like in the works [24, 5], where the case of a point force acting in the
551 x_2 -direction at location $(-0.02, 0.)$ m was considered, a force acting in the x_1 -
552 direction and defined on a segment between two points $(-0.02125, 0.)$ m and
553 $(-0.01875, 0.)$ m is herein applied. The force as a time function is a ricker signal
554 with a central frequency $f_{max} = 170$ kHz and a cutoff frequency $f_c = 425$ kHz.
555 Corresponding to the cutoff frequency, the shortest wavelength (of quasi trans-
556 verse waves) is equal to 4.3mm. Two element sizes, $h_1^E = 1$ mm and $h_2^E = 0.5$ mm,
557 are used here. For the “tDG” solver, the time steps used for these two mesh
558 sizes are respectively $\Delta t_{tDG,1} = 200$ ns and $\Delta t_{tDG,2} = 100$ ns, while, for the
559 “sDG” solver, they are respectively $\Delta t_{sDG,1} = 40$ ns and $\Delta t_{tDG,2} = 20$ ns. The
560 total simulation time is $T = 100\mu$ s.

561 Firstly, four snapshots of evolving quasi longitudinal and quai transverse
562 wave fronts are presented in Figure 3 for a qualitative comparison with the
563 analytically calculated fronts (Figure 2(a)) and the numerical results presented
564 in [24, 5].

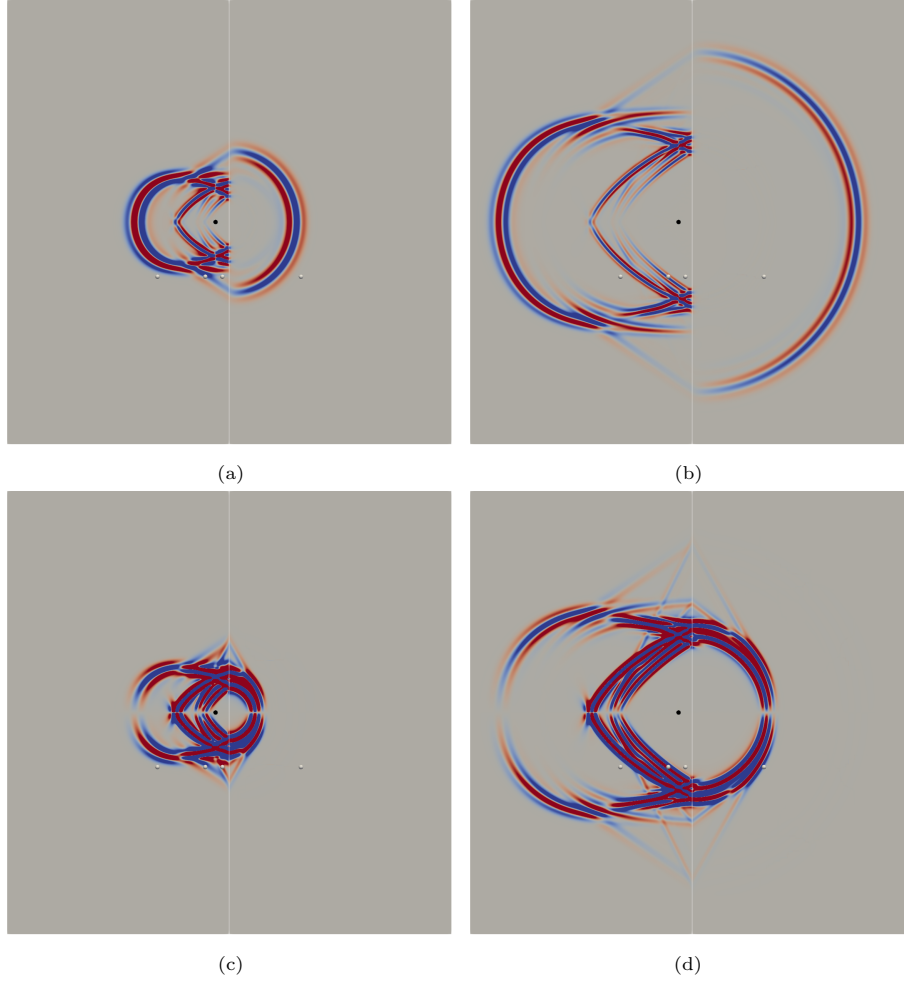


Figure 3: (a) and (b) $\text{div} \mathbf{u}$ respectively at $30\mu\text{s}$ and $60\mu\text{s}$; (c) and (d) $\text{curl} \mathbf{u}$ respectively at $30\mu\text{s}$ and $60\mu\text{s}$. The location of the middle point of the loading segment is indicated by a black circle, and the four sampling locations are indicated by white circles.

565 In our work, the Helmholtz's decomposition is used in the following way
 566 to display quasi longitudinal and quai transverse wave fronts. Displacement
 567 fields are decomposed into two vector fields, the one curl-free and the other one
 568 divergence-free. In the case of isotropic and homogenous elastic media, the curl-
 569 free part \mathbf{u}_L is in fact the longitudinal wave component, as it is solution of the
 570 longitudinal wave equation, while, the divergence-free part \mathbf{u}_T is the transverse
 571 wave component, as it is solution of the transverse wave equation. Therefore,
 572 by displaying the scalar field $\text{div} \mathbf{u}$ ($= \text{div} \mathbf{u}_L$) and the vector field $\text{curl} \mathbf{u}$ ($=$
 573 $\text{curl} \mathbf{u}_T$), longitudinal and transverse wavefronts are respectively represented.
 574 Now, let us consider, in the case of 2D anisotropic and homogeneous elastic

575 media, a quasi longitudinal or a quasi transverse wave of wave vector \mathbf{k} propa-
 576 gating in it: $\mathbf{u} = \mathbf{U}e^{i(\mathbf{k} \cdot \mathbf{x} - \omega t)}$, with $\mathbf{U} = U_{\mathbf{k}}\mathbf{e}_{\mathbf{k}} + U_{\mathbf{k}\perp}\mathbf{e}_{\mathbf{k}\perp}$, where $U_{\mathbf{k}}$ and $U_{\mathbf{k}\perp}$
 577 are the amplitude components respectively parallel and perpendicular to the
 578 wave vector \mathbf{k} , $\mathbf{e}_{\mathbf{k}}$ and $\mathbf{e}_{\mathbf{k}\perp}$ being unit vectors. Then, we have:

$$\operatorname{div}\mathbf{u} = U_{\mathbf{k}}\|\mathbf{k}\|e^{i(\mathbf{k} \cdot \mathbf{x} - \omega t)}, \operatorname{curl}\mathbf{u} = U_{\mathbf{k}\perp}\|\mathbf{k}\|\mathbf{e}_{\mathbf{k}} \times \mathbf{e}_{\mathbf{k}\perp}e^{i(\mathbf{k} \cdot \mathbf{x} - \omega t)} \quad (76)$$

579 Therefore, both fields $\operatorname{div}\mathbf{u}$ and $\operatorname{curl}\mathbf{u}$ can still reveal the quasi longitudinal
 580 wavefronts and the quasi transverse wavefronts. Generally, we have $|U_{\mathbf{k}\perp}| <$
 581 $|U_{\mathbf{k}}|$ on a quasi longitudinal wavefront, and $|U_{\mathbf{k}}| < |U_{\mathbf{k}\perp}|$ on a quasi transverse
 582 wavefront.

583 In Figure 3, both fields $\operatorname{div}\mathbf{u}$ and $\operatorname{curl}\mathbf{u}$ calculated by the space dG solver
 584 with the finer mesh size h_2^E are shown at two moments $30\mu\text{s}$ and $60\mu\text{s}$. Pure longi-
 585 tudinal and transverse wavefronts are observed in the isotropic material, while
 586 quasi longitudinal and transverse wavefronts are observed in the anisotropic
 587 material. The visual comparison to the theoretically predicted wavefronts (Fig-
 588 ure 2(b)), on the one hand, and to the results presented in [24, 5], on the other
 589 hand, shows that the space dG solver correctly solves all propagating phenom-
 590 ena at the physical interface and inside both materials.

591 To carry out a quantitative comparison between the tDG solver and the
 592 sDG solver, we consider displacements recorded at four sample points: $S_1 =$
 593 $(-0.105, -0.08)\text{m}$, $S_2 = (-0.035, -0.08)\text{m}$, $S_3 = (-0.01, -0.08)\text{m}$ and $S_4 =$
 594 $(0.105, -0.08)\text{m}$, as proposed in [5]. In Figure 3, the location of the middle
 595 point of the loading segment is indicated by a black circle, and the four sam-
 596 pling locations are indicated by white circles. Figure 4 show the comparison of
 597 displacement components calculated by the tDG solver and the sDG solver on
 598 the finer mesh, *i.e.*, with $h_2^E = 0.5\text{mm}$. The comparison is good especially for
 599 the (quasi) longitudinal wavefronts, which is completely normal, because the
 600 wavelength of the longitudinal waves is approximately twice as long as that of
 601 the transverse waves. When the comparison is made between the results ob-
 602 tained by using the two different mesh sizes h_1^E and h_2^E (Figure 5), it is worth
 603 noticing that the behavior of the sDG solver is much better than that of the
 604 tDG solver. Indeed, by the tDG solver, the relative error, which is the differ-
 605 ence between the two solutions obtained with respectively h_1^E and h_2^E , is larger,
 606 because it is mainly in the phase of the solution. In other words, the arrival
 607 time of the waves is much more correctly calculated by the sDG solver, even
 608 with the coarser element size h_1^E .

609 5.2. Polycrystalline materials

610 The second example considers the application of the sDG solver to single-
 611 phase and untextured polycrystalline materials in the 2D case and was proposed
 612 in our previous work [8]. We recall that a single-phased polycrystal is an as-
 613 sembly of small single crystals bonded together. Each crystallite (grain) is
 614 anisotropic and they all have the same elastic Hooke tensor but with differently
 615 and randomly oriented basis of anisotropy. Hence, such a polycrystalline ma-
 616 terial is a typical example of piecewise homogeneous media including a large

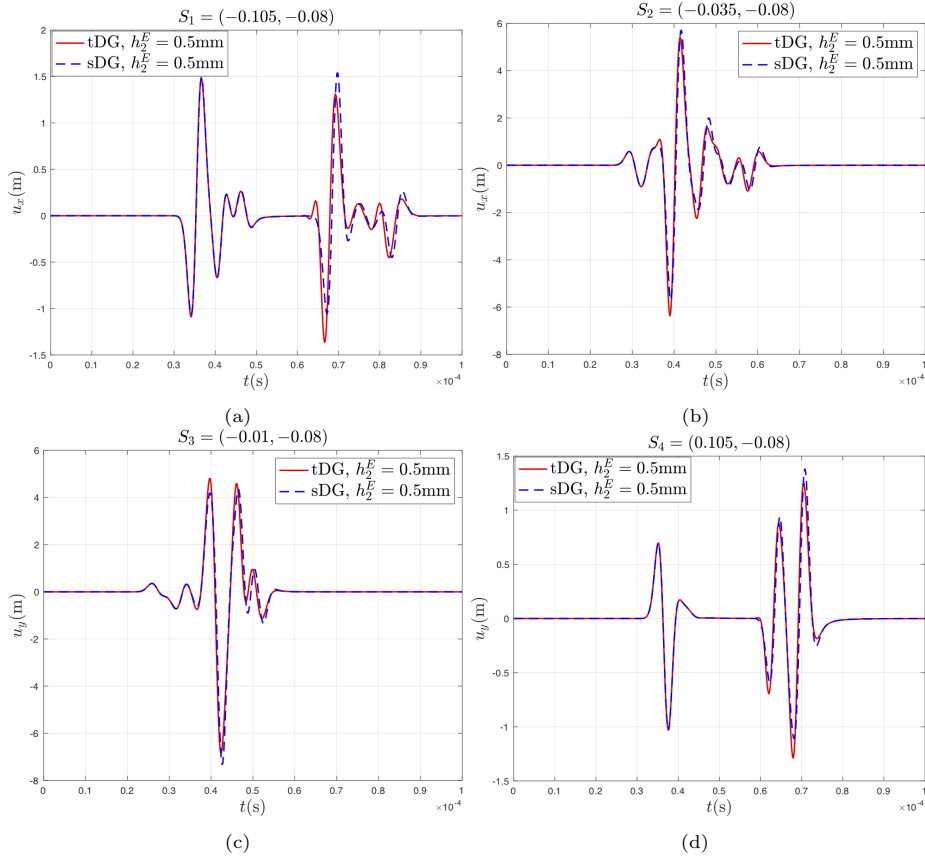


Figure 4: Comparison of displacement components calculated by the tDG solver and the sDG solver on the finer mesh.

617 number of physical interfaces. Elastic waves propagating in it are scattered and
 618 attenuated due to interactions between waves and grain interfaces.

619 In a single-phase polycrystalline material, the degree of inhomogeneity in
 620 elastic properties is completely determined by the degree of anisotropy of the
 621 crystallite's Hooke tensor: the stronger the anisotropy, the higher the degree of
 622 inhomogeneity. In the related literature, it is usually expressed by measuring
 623 its departure from its Voigt average homogeneous equivalent medium in the
 624 following way [25]:

$$\xi_{ijkl}^2 = \frac{1}{4} \frac{\langle (C_{ijkl}(\theta) - C_{ijkl}^{Voigt})^2 \rangle_{\theta}}{\langle (C_{ijkl}^{ref-Voigt})^2 \rangle_{\theta}} \quad (77)$$

625 where, the subscript “ $ijkl$ ” has the proper value for either longitudinal or trans-
 626 verse waves, and $\langle \cdot \rangle_{\theta}$ stands for the average over all orientations of the local
 627 material anisotropic axes denoted by θ .

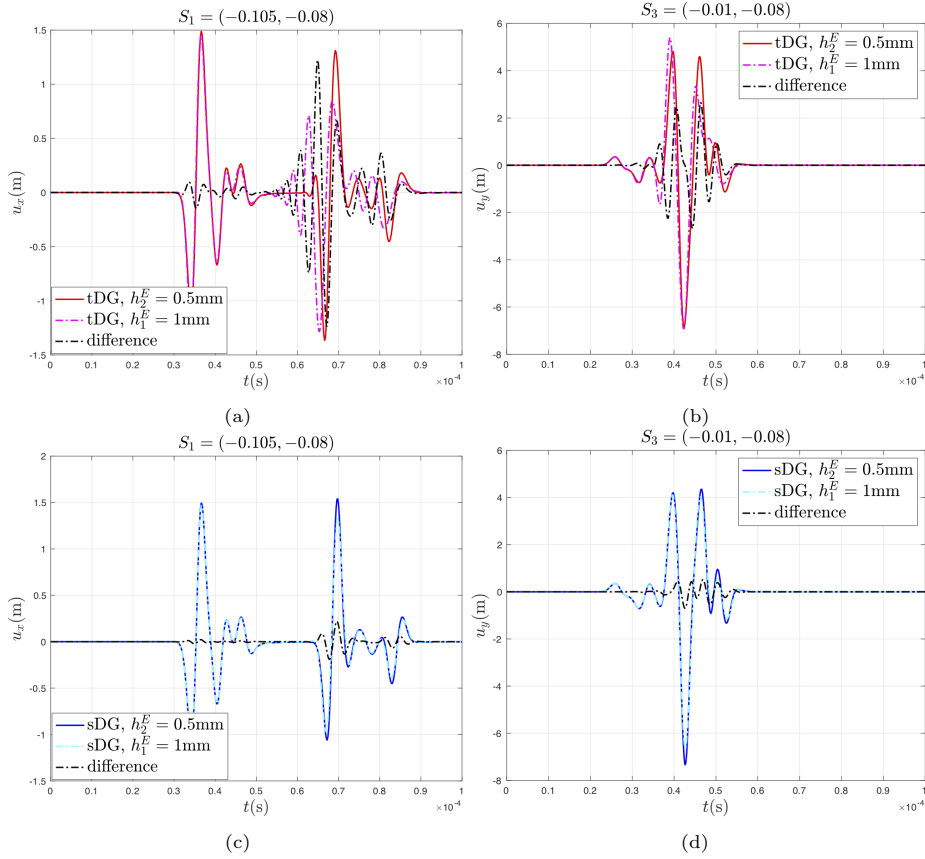


Figure 5: Comparison of displacement components calculated with two different mesh sizes.

628 Each finite element model defined herein is a polycrystal occupying a rectangular
629 domain, and it is composed of 2106 elliptic grains of size $480\mu\text{m} \times 240\mu\text{m}$.
630 The dimensions of the rectangular domain are given in Figure 6(a). The free
631 boundary condition is prescribed on the boundary of the rectangular domain,
632 except that a pressure loading is applied on a segment L_e of length 2.8mm.
633 For the amplitude of the pressure loading, a Gaussian distribution along the
634 segment L_e is chosen in order to reduce as much as possible the generation of
635 transverse waves at the ends of the segment L_e . The period of ricker signal
636 in time of the pressure loadings is $T_r = 0.4\mu\text{s}$, resulting in $f_{max} = 5\text{MHz}$ and
637 $f_c = 12.5\text{MHz}$. Hence, the frequency domain of validation to be considered
638 hereafter ranges from 2MHz to 12.5MHz.

639 Two polycrystals with different degrees of inhomogeneity are considered:

- 640 (1) Reference material denoted by “ref”. It is a titanium alloy with crystallites
641 of cubic symmetry. It is orthotropic and its Hooke tensor is denoted by
642 \mathbf{C}^{ref} .
643 (2) Material denoted by “strong”. To define an orthotropic material with a high

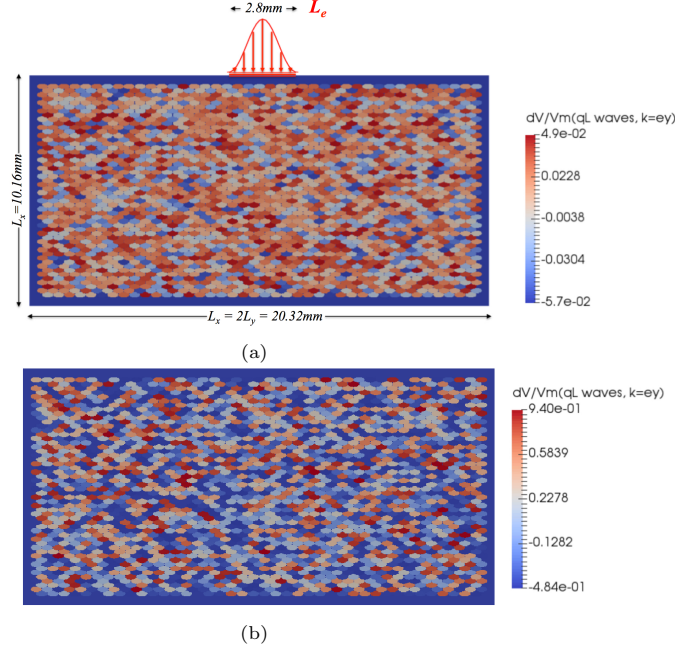


Figure 6: (a) FE model of a single-phase polycrystal composed of elliptic grains with pressure loading applied on the emitter segment L_e with a Gaussian distribution. Dispersions dV/V_m in the phase wave velocity $c_{qL}(\mathbf{k})$ with $\mathbf{k} = \mathbf{e}_y$ for the polycrystals (a) “ref” and (b) “strong”, V_m being the averaged wave velocity $\langle c_{qL}(\mathbf{k}) \rangle_{grains}$ over all grains and $dV = c_{qL}(\mathbf{k}) - V_m$ for each grain.

644 degree of anisotropy, we use the Hooke tensor \mathbf{C}^{strong} of a fiber-reinforced
 645 material.

646 For both materials, their homogenized equivalent media are isotropic and the
 647 corresponding Voigt average Hooke tensors are respectively denoted by $\mathbf{C}^{ref-Voigt}$
 648 and $\mathbf{C}^{strong-Voigt}$. The elastic moduli in the local material anisotropic basis
 649 $(\mathbf{a}_1, \mathbf{a}_2, \mathbf{a}_3)$ of both polycrystals are given in Table II, as well as ξ_L the de-
 650 gree of inhomogeneity. Their densities are respectively $\rho^{ref} = 4428\text{kg.m}^{-3}$ and
 651 $\rho^{strong} = 2710\text{kg.m}^{-3}$.

652 Ten samples with different random distributions $\{\Theta_i\}_{i=0,\dots,9}$ of crystallo-
 653 graphic orientations are considered.

654 As for the choice of numerical parameters, square Q4 elements of size $h =$
 655 $25\mu\text{m}$ are used. This choice leads to have at least about 19 elements in the
 656 shortest quasi-longitudinal wavelength for the cut-off frequency f_c for all the
 657 studied materials, except the material “strong-Voigt” for which this number is
 658 about 12. As the principle results considered are numerical measures of the
 659 attenuation coefficient and of the noise levels of the quasi longitudinal waves,
 660 the finite element size is defined with respect to the shortest quasi longitudinal
 661 wavelength, which is approximately twice the shortest quasi transverse wave-
 662 length. We note that the influence of the finite element size on these numerical

	C_{iiii}	$C_{ijjj,i \neq j}$	$C_{ijij,i \neq j}$	ξ_L			
\mathbf{C}^{ref} (GPa)	134.0	110.0	36.0	0.028			
$\mathbf{C}^{ref-Voigt}$ (GPa)	153.0	100.0	26.5	0			
	C_{1111}	$C_{iiii,i=2,3}$	C_{2233}	$C_{11ii,i=2,3}$	$C_{1i1i,i=2,3}$	C_{2323}	ξ_L
\mathbf{C}^{strong} (GPa)	132.5	10.3	0.4	3.6	4.0	5.0	0.563
$\mathbf{C}^{strong-Voigt}$ (GPa)	35.4	35.4	10.6	10.6	12.4	12.4	0

Table II: Elastic moduli and degrees of inhomogeneity of the studied materials “ref” and “strong”, and their homogenized equivalent media “ref-Voigt” and “strong-Voigt”

663 measures has been studied in [26, 27]. Finally, the time steps are calculated by
664 using the formulas (73) for the sDG solver and (75) for the tDG solver.

665 Numerical results obtained with the use of the flux “MG_sDG” are compared
666 to those calculated by either the tDG solver or the space dG solver with a flux
667 defined by using the Voigt average of Hooke elastic tensor at a physical interface
668 (named “cV_sDG” hereafter). We recall that the flux “cV_sDG” was proposed
669 in [8] and it does not solve exactly the Riemann problem on a physical interface.

670 The quantitative comparison of numerical results obtained by the three
671 solvers “tDG”, “cV_sDG” and “MG_sDG” is made in terms of two numerically
672 evaluated quantities: the attenuation coefficient $\alpha(f)$ in the frequency domain
673 and the backscattered noise levels in the time domain calculated as normalized
674 root-mean-square (rms) noise levels $N_{rms}(f_0; t)$ for a given frequency f_0 . Both
675 quantities are calculated for the longitudinal waves.

676 Firstly, the attenuation coefficient is numerically evaluated in the ten sam-
677 ples in the polycrystal “ref”. In a polycrystal, the attenuation measures the
678 amplitude decay of elastic waves during their propagation and it can be caused
679 by dissipation, geometrical spreading or scattering-induced diffusion. In the
680 present work, only the scattering-induced attenuation is considered, and it is
681 usually quantified by a scalar α , called the attenuation coefficient, which defines
682 an exponential decay law. Numerical calculation of α in the frequency domain
683 is done in the following way [26, 28]: Discrete Fourier Transform is used to
684 decompose the time-series signal of the reflected wave fronts $v_y^r(\mathbf{x}_j, t)$ at the j th
685 probe \mathbf{x}_j into the frequency domain and gives rise to the corresponding ampli-
686 tude spectrum $\hat{v}_y^r(\mathbf{x}_j, f)$. With those data, the attenuation coefficient $\alpha(f)$ as a
687 function of the frequency f is measured as:

$$\alpha(f) = -\frac{10}{D} \ln\left(\frac{\sum_{j=1}^M |\hat{v}_y^r(\mathbf{x}_j, f)|^2}{\sum_{j=1}^M |\hat{v}_y^{r,ref}(\mathbf{x}_j, f)|^2}\right) \quad (78)$$

688 To eliminate the attenuation due to the geometrical spreading of wavefront, the
689 ratio in (78) is calculated with respect to $\hat{v}_y^{r,ref}(\mathbf{x}_j, f)$ the reflected echo signals
690 recorded in the equivalent homogeneous medium instead of the incident signals.
691 In (78), $M = 22$, the constant 10 is for the unit conversion from Neper (Np) to
692 decibel (dB), and D stands for the wave propagation distance just before the
693 arrival of reflected echoes at the probes.

694 Figure 7 presents comparisons between the numerical measurements of atten-
695 tuation in the polycrystal “ref” by the three solvers “tDG”, “cV_sDG” and
696 “MG_sDG”. The attenuation coefficient α is plotted either for the crystallo-
697 graphic orientation distribution Θ_0 (Figure 7(a)) or for all the ten $\{\Theta_i\}_{i=0,\dots,9}$
698 (Figure 7(b)). In the latter case, the averaged measure and the minimum and
699 maximum bounds for all the ten measures are plotted. The numerical mea-
700 surements given by both space dG solvers with two different fluxes are very
701 close, giving a maximum relative difference of 3% for both single and averaged
702 measurements. We note that the polycrystal “strong” is not considered for the
703 attenuation coefficient, because coherent echo signals cannot be recorded due to
the high levels of backscattered noises.

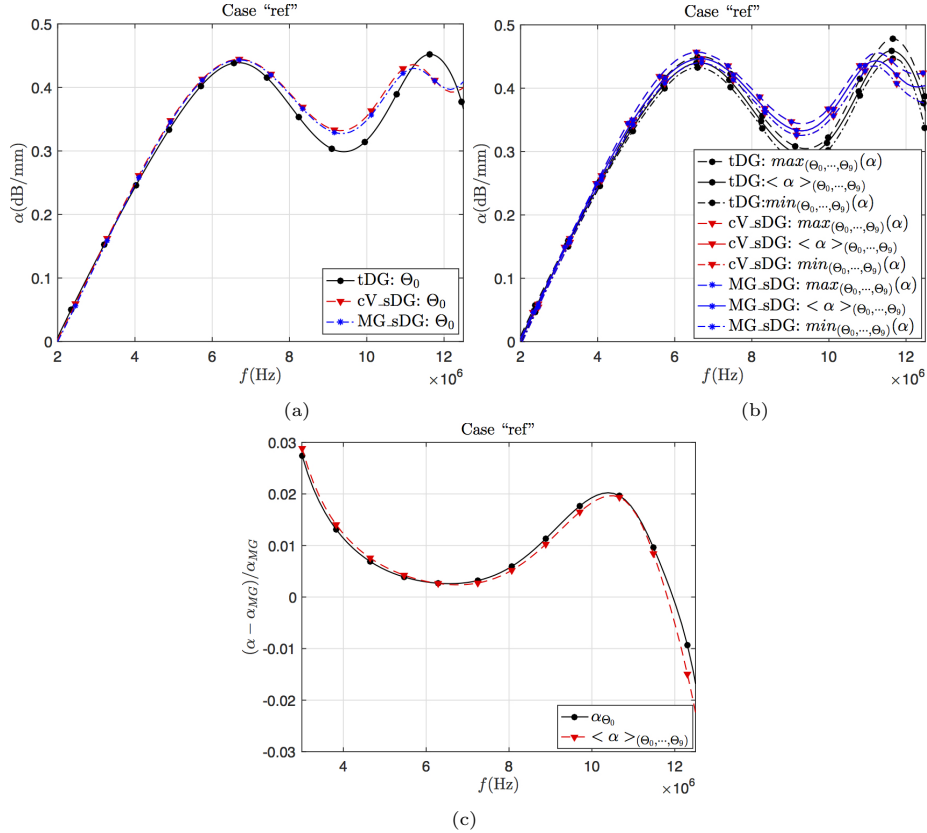


Figure 7: Comparison between three solvers of numerical measurements of the attenuation coefficient α in the polycrystal “ref”. (a) α measured in the sample Θ_0 ; (b) Discrepancies of numerical measure with $mean_{\Theta}(\alpha)$, $min_{\Theta}(\alpha)$ and $max_{\Theta}(\alpha)$ denoting respectively the averaged numerical measures, the minimum and maximum bounds of numerical measures over the ten samples $\Theta_0 - \Theta_9$; (c) Relative differences taking the measurements given by “MG_sDG” as the reference one.

704 Secondly, backscattered noise levels are numerically measured in the time
705 domain for two frequencies $f_0 = 5\text{MHz}$ and 10MHz . We recall that the backscat-
706

707 tered noise levels are numerically measured in the time domain for a given fre-
 708 quency f_0 in terms of normalized root-mean-square (rms) noise levels $N_{rms}(f_0; t)$,
 709 which are defined in the following way [29, 26, 27]:

$$N_{rms}(f_0; t) = \frac{\sqrt{\frac{1}{10 \times M} \sum_{j=1}^{10 \times M} (v_y^b(f_0; \mathbf{x}_j, t) - b(f_0; t))^2}}{E_{max}(f_0)} \quad (79)$$

710 with

$$b(f_0; t) = \frac{1}{10 \times M} \sum_{j=1}^{10 \times M} v_y^b(f_0; \mathbf{x}_j, t) \quad (80)$$

711 where $10 \times M$ means the average is taken over all probes and over all the ten
 712 samples. For a given frequency f_0 , Equation (79) defines in the time domain
 713 the rms positional average of the difference between the noise signal $v_y^b(f_0; \mathbf{x}_j, t)$
 714 and the mean noise level $b(f_0; t)$. The noise signal $v_y^b(f_0; \mathbf{x}_j, t)$ is calculated by
 715 applying a frequency filtering to the noise signal $v_y^b(\mathbf{x}_j, t) = v_y(\mathbf{x}_j, t) - v_y^{ref}(\mathbf{x}_j, t)$
 716 recorded at the j th receiver \mathbf{x}_j . The normalization by $E_{max}(f_0)$ eliminates the
 717 dependence of the noise level on the incident power. $E_{max}(f_0)$ is taken equal to
 718 one half of the peak-to-peak amplitude of the incident signals for the frequency
 719 f_0 , as proposed in [29].

720 Comparisons between the three solvers of the normalized rms noise levels
 721 $N_{rms}(f_0; t)$ in the time domain for the ten samples of the polycrystal “ref”
 722 (*resp.* “strong”) are presented in Figure 8 (*resp.* Figure 9). Backscattered noise
 723 levels evaluated by the two solvers “cV_sDG” and “MG_sDG” are very close.
 724 However, it can be noted that discrepancies between them increase with time
 725 and are more due to a phase shift than to differences in the amplitude. Finally,
 726 it is shown in Figure 10 that the higher the degree of inhomogeneity, the greater
 727 the gap resulting from the use of two different numerical fluxes “cV_sDG” and
 “MG_sDG”.

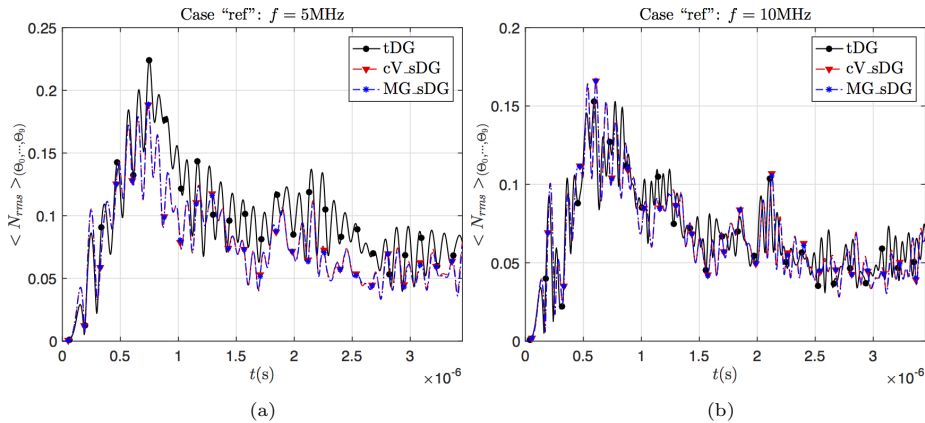


Figure 8: Comparison between three solvers of the normalized rms noise levels $N_{rms}(f_0; t)$ for the ten samples of the polycrystal “ref”. (a) $f_0 = 5\text{MHz}$; (b) $f_0 = 10\text{MHz}$

728

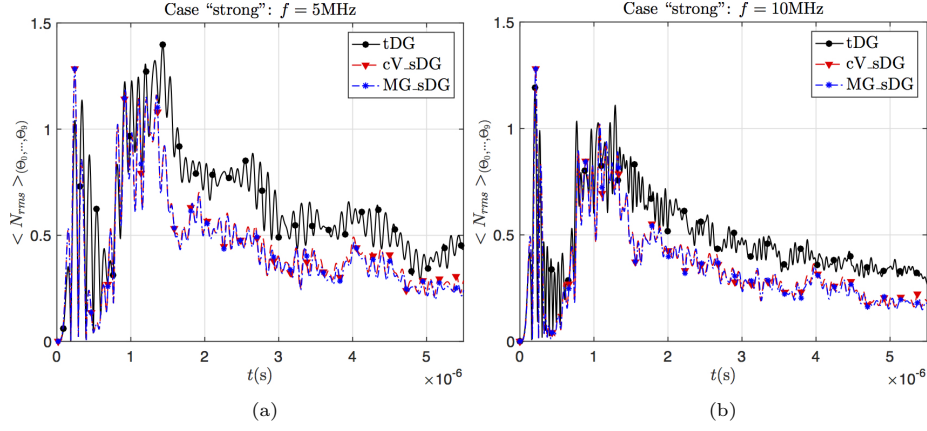


Figure 9: Comparison between three solvers of the normalized rms noise levels $N_{rms}(f_0; t)$ for the ten samples of the polycrystal “strong”. (a) $f_0 = 5\text{MHz}$; (b) $f_0 = 10\text{MHz}$

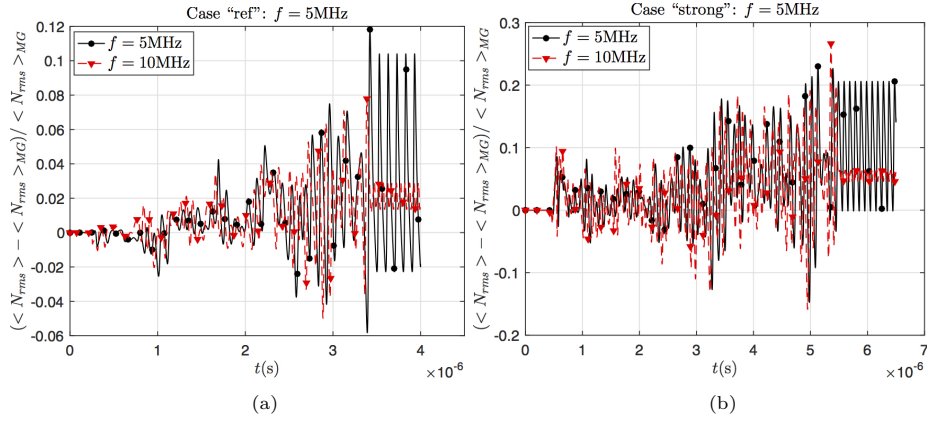


Figure 10: Comparison between both solvers “cV_sDG” and “MG_sDG” of the averaged normalized rms noise levels $N_{rms}(f_0; t)$: relative differences taking the measurements given by “MG_sDG” as the reference one for the polycrystals (a) “ref” and (b) “strong”

6. Conclusions

729 A systematic development of upwind numerical fluxes for the space discontinuous Galerkin method to model elastic wave propagation has been proposed
730 in the most general case of multidimensional anisotropic and heterogeneous media with physical interfaces, *i.e.* interfaces with discontinuous material properties.
731 Within a unified and wave oriented variational framework, both first-order velocity-stress and velocity-strain wave formulations were considered, and upwind
732 numerical fluxes were developed in explicit and intrinsic tensorial expressions. They are approximate or exact solution of a Riemann problem, depending
733 hierarchically on the degree of inhomogeneity across a physical interface. More particularly in the case of the first-order velocity-stress wave formulation, the
734
735
736
737
738
739

740 tricky issue of defining a relevant Riemann problem in order to obtain physically
741 sound interface conditions was discussed and solved. Finally, the upwind nu-
742 merical flux that is exact solution of the appropriately defined Riemann problem
743 was validated by numerical examples involving one or more physical interfaces
744 separating anisotropic materials.

745 As an important remark, the analysis of stability of a space dG method is
746 essential, because of the use of numerical fluxes. A stability analysis has been
747 performed by the author for the velocity-stress wave formulation [30]. At the
748 continuous level of the time and whatever the space dimension, the stability
749 has been proved in the case of an isotropic or anisotropic elastic medium with
750 continuous properties or an isotropic elastic medium with discontinuous prop-
751 erties. But, the stability has been only proved in the 2D case for an anisotropic
752 elastic medium with discontinuous properties satisfying a sufficient condition,
753 which involves the degree of inhomogeneity of physical interfaces. In our current
754 numerical studies, we have not yet encountered any instability problem. But, it
755 is clear that this is an important point to be addressed by future studies.

756 Acknowledgments

757 This work was granted by the ANR (Agence Nationale de la Recherche)
758 - MAPIE project, ANR-13-MONU-002. Computations were performed using
759 HPC resources from the “Mésocentre” computing center of CentraleSupélec and
760 ENS Paris-Saclay.

761 References

- 762 [1] B. Cockburn, G. Karniadakis, C.-W. Shu, (Eds.), Discontinuous Galerkin
763 Methods. Theory, Computation and Applications, Lecture Notes in Com-
764 putational Science and Engineering, volume 11, ISBN-13:978-3-642-
765 64098-8, Springer-Verlag, 2000.
- 766 [2] R. LeVeque, Finite Volume Methods for Hyperbolic Problems, Cambridge
767 Texts in Applied Mathematics, Cambridge University Press, 2002.
- 768 [3] M. Käser, M. Dumbser, An arbitrary high-order discontinuous Galerkin
769 method for elastic waves on unstructured meshes – I. the two-dimensional
770 isotropic case with external source terms, Geophysical Journal Interna-
771 tional 166 (2) (2006) 855–877. doi:10.1111/j.1365-246X.2006.03051.x.
- 772 [4] M. Dumbser, M. Käser, An arbitrary high-order discontinuous Galerkin
773 method for elastic waves on unstructured meshes – II. the three-dimensional
774 isotropic case, Geophysical Journal International 167 (1) (2006) 319–336.
775 doi:10.1111/j.1365-246X.2006.03120.x.
- 776 [5] J. de la Puente, M. Käser, M. Dumbser, H. Igel, An arbitrary high-order
777 discontinuous Galerkin method for elastic waves on unstructured meshes
778 – IV. anisotropy, Geophysical Journal International 169 (3) (2007) 1210–
779 1228. doi:10.1111/j.1365-246X.2007.03381.x.

- 780 [6] L. Wilcox, G. Stadler, C. Burstedde, O. Ghattas, A high-order discontinuous Galerkin method for wave propagation through coupled elastic-acoustic media, *Journal of computational Physics* 229 (2010) 9373–9396. doi:doi:10.1016/j.jcp.2010.09.008.
- 784 [7] N. Dudley Ward, T. Lähivaara, S. Eveson, A discontinuous Galerkin method for poroelastic wave propagation: The two-dimensional case, *Journal of Computational Physics* 350 (2017) 690–727.
- 788 [8] B. Tie, A.-S. Mouronval, V.-D. Nguyen, L. Series, D. Aubry, A unified variational framework for the space discontinuous Galerkin method for elastic wave propagation in anisotropic and piecewise homogeneous media, *Computer Methods in Applied Mechanics and Engineering* 338 (2018) 299–332.
- 792 [9] Q. Zhan, Q. Ren, M. Zhuang, Q. Sun, Q. Liu, An exact Riemann solver for wave propagation in arbitrary anisotropic elastic media with fluid coupling, *Computer Methods in Applied Mechanics and Engineering* 329 (2018) 24–39.
- 796 [10] Q. Zhan, M. Zhuang, Y. Mao, Q. Liu, Unified Riemann solution for multiphysics coupling: Anisotropic poroelastic/elastic/fluid interfaces, *Journal of Computational Physics* 402 (2020) 108961.
- 798 [11] T. Warburton, A low-storage curvilinear discontinuous Galerkin method for wave problems, *SIAM J. Sci. Comput.* 35 (4) (2013) A1987–A2012.
- 800 [12] R. Ye, M. de Hoop, C. Petrovitch, L. Pyrak-Nolte, L. Wilcox, A discontinuous Galerkin method with a modified penalty flux for the propagation and scattering of acousto-elastic waves, *Geophysical Journal International* 205 (2016) 1267–1289.
- 804 [13] J. Chan, Weight-adjusted discontinuous Galerkin methods: Matrix-valued weights and elastic wave propagation in heterogeneous media, *International Journal for Numerical Methods in Engineering* 113(12) (2018) 1779–1809.
- 808 [14] K. Shukla, J. Chan, M. de Hoop, P. Jaiswal, A weight-adjusted discontinuous Galerkin method for the poroelastic wave equation: Penalty fluxes and micro-heterogeneities, *Journal of Computational Physics* 403 (2020) 109061.
- 811 [15] E. Toro, *Riemann Solvers and Numerical Methods for Fluid Dynamics: A Practical Introduction*, Springer, 2009.
- 813 [16] B. Cockburn, C.-W. Shu, Runge-Kutta Discontinuous Galerkin Methods for Convection-Dominated Problems, *J. Sci. Comput.* 16 (3) (2002) 173–261.
- 816 [17] T. J. Hughes, G. Hulbert, Space-time finite element methods for elastodynamics: Formulations and error estimates, *Computer Methods in Applied Mechanics and Engineering* 66 (1988) 339–363.

- 819 [18] C. Johnson, Discontinuous Galerkin finite element methods for second order
820 hyperbolic problems, *Computer Methods in Applied Mechanics and*
821 *Engineering* 107 (1993) 117–129.
- 822 [19] M. Li, N. Wiberg, Implementation and adaptivity of space-time finite ele-
823 ment method for structural dynamics, *Computer Methods in Applied Me-*
824 *chanics and Engineering* 156 (1998) 211–229.
- 825 [20] B. Tie, D. Aubry, Adaptive time discontinuous Galerkin method for nu-
826 merical modeling of wave propagation in shell and 3D structures, *European*
827 *Journal of computational Mechanics* 15 (6) (2006) 729–757.
- 828 [21] J.-M. Leclère, Parallel and adaptive FE modeling of elastic wave propaga-
829 tion in structures (Modélisation parallèle de la propagation d’ondes dans
830 les structures par éléments finis adaptatifs), Ph.D. thesis, École Centrale
831 de Paris (in French) (2001).
- 832 [22] A. Grédé, Numerical modeling of pyrotechnic shock wave propagation in
833 Ariane5’s structures (Modélisation des chocs d’origine pyrotechnique dans
834 les structures d’Ariane5 : Développement de modèles de propagation et
835 d’outils de modélisation), Ph.D. thesis, École Centrale de Paris (in French)
836 (2009).
- 837 [23] T. Ekevid, M. X. Li, N. Wiberg, Adaptive FEA of wave propagation in-
838 duced by high-speed trains, *Computers and Structures* 79 (2001) 2693–
839 2704.
- 840 [24] D. Komatitsch, C. Barnes, J. Tromp, Simulation of anisotropic wave prop-
841 agation based upon a spectral element method, *Geophysics* 65 (2000) 1251–
842 1260.
- 843 [25] F. E. Stanke, G. S. Kino, A unified theory for elastic wave-propagation
844 in polycrystalline materials, *Journal of the Acoustical Society of America*
845 75(3) (1984) 665–681.
- 846 [26] X. Bai, Finite element modeling of ultrasonic wave propagation in poly-
847 crystalline materials, Ph.D. thesis, CentraleSupélec (2017).
848 URL <https://tel.archives-ouvertes.fr/tel-01483701/document>
- 849 [27] X. Bai, B. Tie, J.-H. Schmitt, D. Aubry, Finite element modeling of grain
850 size effects on the ultrasonic microstructural noise backscattering in poly-
851 crystalline materials, *Ultrasonics* 87 (2018) 182–202.
- 852 [28] X. Bai, B. Tie, J.-H. Schmitt, D. Aubry, Comparison of ultrasonic at-
853 tenuation within two- and three-dimensional polycrystalline media, *Ul-*
854 *trasonics* 100 (2020 (Available online 19 August 2019)) 105980, <https://doi.org/10.1016/j.ultras.2019.105980>.

- 856 [29] F. Margetan, R. Thompson, I. Yalda-Mooshabad, Backscattered mi-
857 crostructural noise in ultrasonic toneburst inspections, *Journal of Nonde-*
858 *structive Evaluation* 13(3) (1994) 111–136.
- 859 [30] B. Tie, Some comparisons and analyses of time or space discontinuous
860 Galerkin methods applied to elastic wave propagation in anisotropic and
861 heterogeneous media, *Advanced Modeling and Simulation in Engineering*
862 *Sciences* 6 (3) (2019) 1–27.

863 Appendix A1

864 *Proof of Theorem 3.1.* By adding the three equations of (21), *i.e.* Eq.(21a) +
865 Eq.(21b) + Eq.(21c), we get:

$$\mathbf{A}_n(\mathbf{U}_h) - \alpha_k \lambda_{\mathbf{n},k}^- \mathbf{R}_{\mathbf{n},k}^- + \mathbf{A}'_{n'}(\mathbf{U}'_h) - \alpha'_k \lambda_{\mathbf{n}',k}^- \mathbf{R}_{\mathbf{n}',k}^- = \mathbf{0} \quad (81)$$

According to the definition of the Jacobian operator (6), the eigenmodes (16)
and the definition (18) and the property (17) of the Christoffel tensor $\mathbf{\Gamma}_n$, we
obtain the following equations by considering separately \wp_{vect} (Eq.(81)) and
 $\mathbf{n} \cdot \wp_{tens}$ (Eq.(81)):

$$\frac{\boldsymbol{\sigma}_h \cdot \mathbf{n}}{\rho} + \frac{\boldsymbol{\sigma}'_h \cdot \mathbf{n}'}{\rho'} = - \sum_l \frac{\alpha_l}{\rho} z_{\mathbf{n},l}^- \frac{\gamma_{\mathbf{n},l}}{\sqrt{2}} - \sum_l \frac{\alpha'_l}{\rho'} z_{\mathbf{n}',l}^- \frac{\gamma'_{\mathbf{n}',l}}{\sqrt{2}} \quad (82a)$$

$$\rho \mathbf{\Gamma}_n \cdot \mathbf{v}_h - \rho' \mathbf{\Gamma}'_{n'} \cdot \mathbf{v}'_h = \sum_l \frac{\alpha_l}{\rho} (z_{\mathbf{n},l}^-)^2 \frac{\gamma_{\mathbf{n},l}}{\sqrt{2}} - \sum_l \frac{\alpha'_l}{\rho'} (z_{\mathbf{n}',l}^-)^2 \frac{\gamma'_{\mathbf{n}',l}}{\sqrt{2}} \quad (82b)$$

866 We recall that the sum is taken over $l = qL, qT_1, qT_2$ and for the sake of clarity
867 the symbol of summation \sum_l is explicitly added in (82). (82) is a linear system
868 of six equations for six unknowns $\{\alpha_k, \alpha'_k\}$. Then, to obtain the expressions
869 given in Theorem 3.1, the following manipulations of (82) are made:

- 870 • For first three equations corresponding to $\{\alpha_k\}$

871 $\frac{\overline{z_{\mathbf{n},k}^-}^R}{z_{\mathbf{n}',k}^-} \frac{\gamma_{\mathbf{n},k}}{\sqrt{2}} \cdot \left(- \frac{z_{\mathbf{n}',k}^-}{\rho^{-1}(z_{\mathbf{n},k}^-)^2} \text{Eq.(82a)} + \frac{1}{\rho^{-1}(z_{\mathbf{n},k}^-)^2} \text{Eq.(82b)} \right)$ results into:

$$*\mathbf{L}_{\mathbf{n},k}^- \cdot \mathbf{U}_h - **\mathbf{L}_{\mathbf{n},k}^- \cdot \mathbf{U}'_h = \alpha_k + \frac{1}{2} \sum_{l \neq k} \left(\frac{\overline{z_{\mathbf{n},k}^-}^R}{z_{\mathbf{n},k}^-} \frac{\rho}{\rho'} \frac{z_{\mathbf{n}',l}^- \delta z_{\mathbf{n}',kl}^-}{z_{\mathbf{n},k}^- z_{\mathbf{n}',k}^-} \gamma_{\mathbf{n},k} \cdot \gamma'_{\mathbf{n}',l}} \right) \alpha'_l \quad (83)$$

- 872 • For the last three equations corresponding to $\{\alpha'_k\}$

873 $\frac{\overline{z_{\mathbf{n},k}^-}^R}{z_{\mathbf{n},k}^-} \frac{\gamma'_{\mathbf{n}',k}}{\sqrt{2}} \cdot \left(- \frac{z_{\mathbf{n},k}^-}{\rho'^{-1}(z_{\mathbf{n}',k}^-)^2} \text{Eq.(82a)} - \frac{1}{\rho'^{-1}(z_{\mathbf{n}',k}^-)^2} \text{Eq.(82b)} \right)$ results into:

874 $*\mathbf{L}'_{\mathbf{n}',k} \cdot \mathbf{U}'_h - **\mathbf{L}'_{\mathbf{n}',k} \cdot \mathbf{U}_h = \alpha'_k + \frac{1}{2} \sum_{l \neq k} \left(\frac{\overline{z_{\mathbf{n},k}^-}^R}{z_{\mathbf{n}',k}^-} \frac{\rho'}{\rho} \frac{z_{\mathbf{n},l}^- \delta z_{\mathbf{n},kl}^-}{z_{\mathbf{n}',k}^- z_{\mathbf{n},k}^-} \gamma'_{\mathbf{n}',k} \cdot \gamma_{\mathbf{n},l}} \right) \alpha_l$ (84)

875 The matrix form of (83) and (84) gives rise to (26). \square

876 Appendix A2

877 *Lemma A2.1.* In the case of continuous material properties, the following equa-
878 tions hold on the interface of elements E and E' :

$$\lambda'_{\mathbf{n}',k} = \lambda_{\mathbf{n},k}, \mathbf{R}_{\mathbf{n}',k}^{\mp'} = -\mathbf{R}_{\mathbf{n},k}^{\pm}, \mathbf{L}_{\mathbf{n}',k}^{\mp'} = -\mathbf{L}_{\mathbf{n},k}^{\pm} \quad (85)$$

879 *Proof.* As the material properties are continuous, we have $\Gamma_{\mathbf{n}} = \Gamma'_{\mathbf{n}'}$, so $\lambda'_{\mathbf{n}',k} =$
880 $\lambda_{\mathbf{n},k}$. Otherwise, by recalling (16), it can be verified that:

$$\begin{aligned} \mathbf{R}_{\mathbf{n},k}^{\pm} &= \begin{pmatrix} \mathbf{w}_{\mathbf{n},k} \\ -\rho(z_{\mathbf{n},k}^{\pm})^{-1} \mathbf{C} : (\mathbf{n} \otimes_s \mathbf{w}_{\mathbf{n},k}) \end{pmatrix} \\ &= \begin{pmatrix} -\mathbf{w}_{\mathbf{n}',k} \\ -\rho'(z_{\mathbf{n}',k}^{\pm'})^{-1} \mathbf{C}' : (\mathbf{n}' \otimes_s \mathbf{w}_{\mathbf{n}',k}) \end{pmatrix} \\ &= - \begin{pmatrix} \mathbf{w}_{\mathbf{n}',k} \\ -\rho'(z_{\mathbf{n}',k}^{\mp'})^{-1} \mathbf{C}' : (\mathbf{n}' \otimes_s \mathbf{w}_{\mathbf{n}',k}) \end{pmatrix} \\ &= -\mathbf{R}_{\mathbf{n}',k}^{\pm'} \end{aligned} \quad (86)$$

881 $\mathbf{L}_{\mathbf{n}',k}^{\mp'} = \mathbf{L}_{\mathbf{n},k}^{\pm}$ can be verified in the same way. \square

882 Appendix A3

883 *Proof of Theorem 3.4.* By adding the three equations of (43), *i.e.* Eq.(43a) +
884 Eq.(43b) + Eq.(43c), we get:

$$\tilde{\mathbf{A}}_{\mathbf{n}}(\mathbf{U}_h) - \tilde{\alpha}_k \lambda_{\mathbf{n},k}^- \tilde{\mathbf{M}}(\mathbf{R}_{\mathbf{n},k}^-) + \tilde{\mathbf{A}}'_{\mathbf{n}'}(\mathbf{U}'_h) - \tilde{\alpha}'_k \lambda_{\mathbf{n}',k}^- \tilde{\mathbf{M}}'(\mathbf{R}_{\mathbf{n}',k}^-) = \mathbf{0} \quad (87)$$

According to the definition of $\tilde{\mathbf{A}}_{\mathbf{n}}$ (45), the eigenmodes (16) and the equation (46), we obtain the following equations by considering separately \wp_{vect} (Eq.(87)) and \wp_{tens} (Eq.(87)):

$$\boldsymbol{\sigma}_h \cdot \mathbf{n} + \boldsymbol{\sigma}'_h \cdot \mathbf{n}' = - \sum_l \tilde{\alpha}_l z_{\mathbf{n},l}^- \frac{\gamma_{\mathbf{n},l}}{\sqrt{2}} - \sum_l \tilde{\alpha}'_l z_{\mathbf{n}',l}^- \frac{\gamma'_{\mathbf{n}',l}}{\sqrt{2}} \quad (88a)$$

$$\mathbf{v}_h - \mathbf{v}'_h = \sum_l \tilde{\alpha}_l \frac{\gamma_{\mathbf{n},l}}{\sqrt{2}} - \sum_l \tilde{\alpha}'_l \frac{\gamma'_{\mathbf{n}',l}}{\sqrt{2}} \quad (88b)$$

885 To obtain (88b), we have used the fact that $\mathbf{w} \otimes_s \mathbf{n} = \mathbf{0}$ implies $\mathbf{w} = \mathbf{0}$.

886 Then, to obtain the expressions given in Theorem 3.4, the following manip-
887 ulations of (88) are made:

- For the first three equations corresponding to $\{\tilde{\alpha}_k\}$

888 $\frac{\overline{z_{\mathbf{n},k}}}{z_{\mathbf{n},k}} \frac{\overline{\gamma_{\mathbf{n},k}}}{\sqrt{2}} \cdot (-\frac{1}{z_{\mathbf{n}',k}} \text{Eq.}(88a) + \text{Eq.}(88b))$ leads to:

$$\overline{\mathbf{L}_{\mathbf{n},k}} \cdot (\mathbf{U}_h - \mathbf{U}'_h) = \tilde{\alpha}_k - \frac{1}{2} \sum_{l \neq k}^{\overline{R}} \left(\frac{\overline{z_{\mathbf{n},k}}}{z_{\mathbf{n},k}} \frac{\delta z_{\mathbf{n}',kl}}{z_{\mathbf{n}',k}} \overline{\gamma_{\mathbf{n},k}} \cdot \overline{\gamma'_{\mathbf{n}',l}} \right) \alpha'_l \quad (89)$$

- For the last three equations corresponding to $\{\tilde{\alpha}'_k\}$

890 $\frac{\overline{z_{\mathbf{n},k}}}{z_{\mathbf{n}',k}} \frac{\overline{\gamma'_{\mathbf{n}',k}}}{\sqrt{2}} \cdot (-\frac{1}{z_{\mathbf{n},k}} \text{Eq.}(88a) + \text{Eq.}(88b))$ leads to:

$$\overline{\mathbf{L}'_{\mathbf{n}',k}} \cdot (\mathbf{U}'_h - \mathbf{U}_h) = \tilde{\alpha}'_k - \frac{1}{2} \sum_{l \neq k}^{\overline{R}} \left(\frac{\overline{z_{\mathbf{n},k}}}{z_{\mathbf{n}',k}} \frac{\delta z_{\mathbf{n},kl}}{z_{\mathbf{n},k}} \overline{\gamma'_{\mathbf{n}',k}} \cdot \overline{\gamma_{\mathbf{n},l}} \right) \alpha_l \quad (90)$$

892 The matrix form of (89) and (90) gives rise to (49). \square

893 Appendix A4

894 *Proof of Theorem 4.1.* By adding the three equations of (62), i.e. Eq.(62a) +
895 Eq.(62b) + Eq.(62c), we get:

$$\mathbf{A}_{\mathbf{n}}(\mathbf{U}_h) - \alpha_k \lambda_{\mathbf{n},k}^- \mathbf{M}(\mathbf{R}_{\mathbf{n},k}^-) + \mathbf{A}'_{\mathbf{n}'}(\mathbf{U}'_h) - \alpha'_k \lambda_{\mathbf{n}',k}' \mathbf{M}'(\mathbf{R}_{\mathbf{n}',k}') = \mathbf{0} \quad (91)$$

According to the definition of $\mathbf{A}_{\mathbf{n}}$ (13) and the eigenmodes (16), we obtain the following equations by considering separately \wp_{vect} (Eq.(91)) and \wp_{tens} (Eq.(91)):

$$(\mathbf{C} : \varepsilon_h) \cdot \mathbf{n} + (\mathbf{C}' : \varepsilon'_h) \cdot \mathbf{n}' = - \sum_l \alpha_l z_{\mathbf{n},l}^- \frac{\overline{\gamma_{\mathbf{n},l}}}{\sqrt{2}} - \sum_l \alpha'_l z_{\mathbf{n}',l}' \frac{\overline{\gamma'_{\mathbf{n}',l}}}{\sqrt{2}} \quad (92a)$$

$$\mathbf{v}_h - \mathbf{v}'_h = \sum_l \alpha_l \frac{\overline{\gamma_{\mathbf{n},l}}}{\sqrt{2}} - \sum_l \alpha'_l \frac{\overline{\gamma'_{\mathbf{n}',l}}}{\sqrt{2}} \quad (92b)$$

896 As for (88b), the fact that $\mathbf{w} \otimes_s \mathbf{n} = \mathbf{0}$ implies $\mathbf{w} = \mathbf{0}$ is used to obtain (92b).

897 It is interesting to remark that (92) is identical to (88) if we change $\mathbf{C} : \varepsilon_h$ with

898 $\boldsymbol{\sigma}_h$.

899 Then, to obtain the expressions given in Theorem 4.1, the following manip-
900 ulations of (92) are made:

- For the first three equations corresponding to $\{\alpha_k\}$

902 $\frac{\overline{z_{\mathbf{n},k}}}{z_{\mathbf{n},k}} \frac{\overline{\gamma_{\mathbf{n},k}}}{\sqrt{2}} \cdot (-\frac{1}{z_{\mathbf{n}',k}} \text{Eq.}(92a) + \text{Eq.}(92b))$ leads to:

$$\mathbf{M}(\overline{\mathbf{L}_{\mathbf{n},k}}) \cdot (\mathbf{U}_h - \mathbf{U}'_h) = \alpha_k - \frac{1}{2} \sum_{l \neq k}^{\overline{R}} \left(\frac{\overline{z_{\mathbf{n},k}}}{z_{\mathbf{n},k}} \frac{\delta z_{\mathbf{n}',kl}}{z_{\mathbf{n}',k}} \overline{\gamma_{\mathbf{n},k}} \cdot \overline{\gamma'_{\mathbf{n}',l}} \right) \alpha'_l \quad (93)$$

903 • For the last three equations corresponding to $\{\alpha'_k\}$
 904 $\frac{\overline{z_{\mathbf{n},k}}^R}{z_{\mathbf{n}',k}} \frac{\gamma'_{\mathbf{n}',k}}{\sqrt{2}} \cdot \left(-\frac{1}{z_{\mathbf{n},k}} \text{Eq.}(92\text{a}) + \text{Eq.}(92\text{b})\right)$ leads to:

$$M'(\mathbf{L}_{\mathbf{n}',k}^{\prime}) \cdot (\mathbf{U}'_h - \mathbf{U}_h) = \alpha'_k - \frac{1}{2} \sum_{l \neq k} \left(\frac{\overline{z_{\mathbf{n},k}}^R}{z_{\mathbf{n}',k}} \frac{\delta z_{\mathbf{n},kl}^-}{z_{\mathbf{n},k}} \gamma'_{\mathbf{n}',k} \cdot \gamma_{\mathbf{n},l} \right) \alpha_l \quad (94)$$

905 The matrix form of (93) and (94) gives rise to (65). □